1.39 Electronic Retinal Prostheses

Daniel Palanker, Department of Ophthalmology, Hansen Experimental Physics Laboratory, Stanford University, Stanford, CA, United States

1.39.1 Abstract

Retinal prostheses are a promising means for restoring sight to patients blinded by the gradual atrophy of photoreceptors in retinal degeneration. They introduce information into the visual system by electrical stimulation of the inner retinal neurons. Subretinal implants stimulate the first layer of neurons after the lost photoreceptors, primarily bipolar cells, which then transfer responses to the ganglion cells via retinal neural network. Therefore, many features of the natural retinal signal processing are preserved in this approach. Epiretinal implants stimulate primarily the ganglion cells, and hence encode visual information is the spiking patterns, which ideally, should match the target cell types. Recent clinical trial with subretinal photovoltaic array demonstrated that acuity of prosthetic vision can reach the pixel pitch of 100 μm, while preclinical measurements achieved grating acuity down to 50 μm. Higher density arrays are now being developed for restoration of central vision in patients blinded by age-related macular degeneration. This chapter reviews the concepts and technologies, preclinical characterization of prosthetic vision and clinical outcomes with the current systems and provides an outlook into the future developments.

1.39.2 Introduction

Retinal degenerative diseases resulting in the progressive loss of photoreceptors are the leading cause of incurable blindness today (Smith et al., 2001). While photoreceptors in retinal degeneration are lost, the inner retinal neurons survive to a large extent (Mazzoni et al., 2008; Humayun et al., 1999; Kim et al., 2002). Retinal prostheses are designed to reintroduce visual information into the neural system by stimulating the surviving retinal neurons electrically. Several such systems have been evaluated in clinical trials, and more advanced technologies are being developed. This review summarizes various approaches to retinal implants, and discusses the challenges and perspectives associated with electronic restoration of sight.

1.39.2.1 Retina Encodes Visual Information

Vision begins with the projection of spatio-temporal patterns of incident light by the cornea and lens onto a thin layer of tissue lining the back of the eye - the retina. This light-sensitive extension of the central nervous system consists of three neural layers: photoreceptors, the inner nuclear layer and the ganglion cell layer (**Fig. 1**A and B).

Photoreceptors are graded-response neurons (i.e., they do not generate action potentials) that transduce photons into changes in their membrane potential by means of light-sensitive proteins, called opsins. The vertebrate retina is inverted, so that photoreceptors are located at the back of the eye in contact with the retinal pigment epithelium (RPE), which is essential to the health and function of the photoreceptors. Among other functions, RPE regenerates photopigments and digests outer segments shed by photoreceptors. Without support from the RPE cells, photoreceptor cells progressively atrophy and die.

The human retina contains about 120 million photoreceptors. Cones dominate the central regions of the visual field and are responsible for day vision. Rods dominate the periphery and mediate night vision. Primates and humans have three distinct cone subtypes in their eyes, called S, M and L (for Short, Medium and Long wavelength) cones. S cones are mostly sensitive to the blue component of the visible light spectrum. M and L cones exhibit significantly overlapping peaks of sensitivity in the middle of the visible light spectrum (M), and toward the longer end of the spectrum (L) (Wandell, 1995).

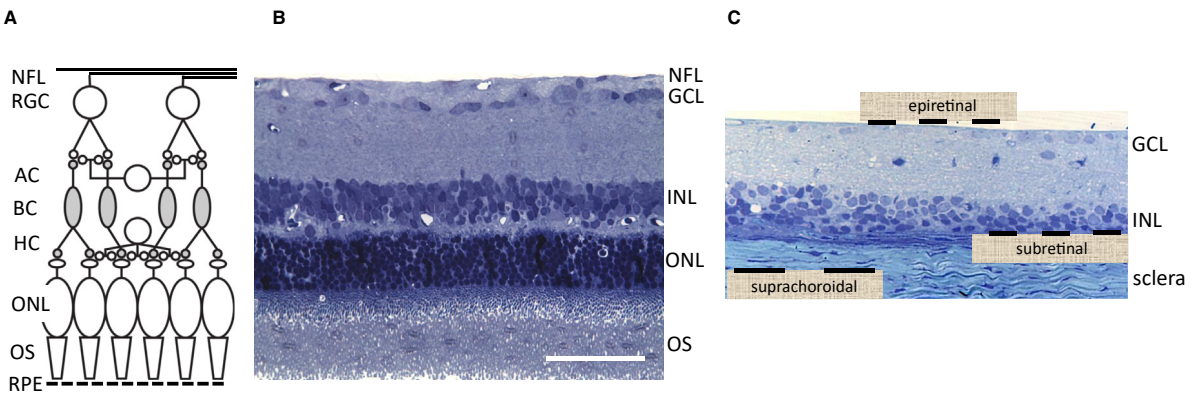

Figure 1 **Retina and the Implant Placement.** (A) Simplified wiring diagram of the retina. Signals from the photoreceptors (composed of nuclei in the outer nuclear layer, ONL, inner and outer segments (OS)) are processed and relayed by the horizontal (HC), bipolar (BC) and amacrine cells (AC) located in the inner nuclear layer (INL) to the retinal ganglion cells (RGC). The axons of the retinal ganglion cells form the nerve fiber layer (NFL), which relays visual signals to the brain. Photoreceptors are located at the back of the eye, in contact with the retinal pigment epithelium (RPE). (B) Histological cross-section of a healthy rat retina. Scale bar: 50 μm. (C) Histological cross-section of a degenerate rat retina (RCS). Epiretinal implants are above the ganglion cell layer. Subretinal implants approach the inner nuclear layer from below (the former photoreceptor side). Suprachoroidal implants are placed below the choroid, into the sclera.

Photoreceptors relay visual information to the neurons in the inner nuclear layer of the retina, composed of about 10 million cells in a human eye, where two types of horizontal cells, about 12 types of bipolar cells, and as many as 30 types of amacrine cells (Masland, 2001; Wassle, 2004) process the visual signals. Retinal interneurons are primarily non-spiking, even though amacrine cells can produce action potentials (Greschner et al., 2014). Retinal interneurons pass on visual information to about 20 distinct classes of retinal ganglion cells (RGCs, about 1 million in a human eye) that generate action potentials relayed to the brain via their axons, which constitute the optic nerve.

Most RGCs encode visual information over a spatially limited region, called their receptive field, which consists of a central area, called the center, and a surrounding ring, called the surround. Retinal ganglion cells that respond to increments of light over the center of their receptive field are called ON ganglion cells, while the ones that respond to light decrements over the center are called OFF ganglion cells. The surround is antagonistic to the center, which means that ON-center ganglion cells have OFF surround, and vice-versa. Ganglion cells can also have spectral opponency properties, such as the blue-ON, yellow-OFF small bistratified cells (Field et al., 2007). In the primate retina, midget ganglion cells have been hypothesized to be responsible for high acuity vision, and the parasol ganglion cells project to areas of the brain thought to encode motion (Salzman et al., 1990; Britten et al., 1992; Merigan and Maunsell, 1993). In many species, including rodents and primates, direction-selective ganglion cells respond to visual motion in a preferred direction (Barlow et al., 1964; Vaney et al., 2012; Manookin et al., 2018), and object-motion sensitive cells are able to segregate motion of the objects from that of background (Olveczky et al., 2003). Bipolar cells relay visual information from the photoreceptors making up the center of the receptive field to ganglion cells. Horizontal cells modulate the synapses between photoreceptors and bipolar cells and are involved in contrast adaptation and in mediating part of the antagonistic center-surround effect. Amacrine cells regulate the synapses between bipolar and ganglion cells and are also involved in center-surround effects by providing lateral inhibition in the retinal network. Starburst amacrine cells are at the heart of the motion direction-selectivity tuning (Briggman et al., 2011). Many other amacrine cell functions in shaping the complex computations in the retina are still under debate in the visual neuroscience community.

1.39.2.2 Retinal Degeneration and Its Effects on the Visual System

The leading cause of incurable blindness in the developed world today is a broad category of diseases known as retinal degeneration (Smith et al., 2001; Haim, 2002). In these conditions, the photoreceptors progressively die, eventually leading to loss of sight. However, neurons in the inner nuclear and ganglion cell layer survive to a large extent and can be stimulated electrically, making them target candidates for retinal prosthetics (**Fig. 1**C).

1.39.2.2.1 Age-Related Macular Degeneration

Age-related macular degeneration (AMD) is a leading cause of untreatable vision loss, affecting over 8.7% of the population worldwide and the number is projected to reach 196 million by 2020 (Wong et al., 2014). Advanced forms of AMD (neovascularization and geographic atrophy) are associated with severe visual impairment, and their prevalence dramatically increases with age: from 1.5% in US population above 40 years to more than 15% in population older than 80 (Friedman et al., 2004).

As AMD progresses, the retinal pigment epithelium cells deteriorate, forming cellular debris called drusen between the pigment epithelium and Bruch's membrane, which separates the RPE from the choroid. Drusen are thought to impede the transport of nutrients from the choroid and tend to grow over time. Eventually, the disease evolves into one of the two advanced forms: in the dry form of advanced AMD, RPE cells in the center of the visual field can begin to atrophy, which leads to the death of the photoreceptors above them. This condition is called geographic atrophy, and it results in the formation of a central blind spot, called a scotoma. Since visual acuity in human eye rapidly drops with eccentricity (Wandell, 1995), loss of central vision, responsible for high-resolution, severely impairs reading and face recognition, while preserved low-resolution peripheral vision allows for normal ambulation. Therefore, restoration of central vision in such condition should provide functional visual acuity and enable central fixation, without jeopardizing the surrounding retina.

Another form of advanced AMD, called the wet or neovascular form, involves the growth of new blood vessels from the choroid into the retina, which degrades central vision. Anti-angiogenic drugs can block the signaling pathway of the Vascular Endothelial Growth Factor (VEGF) and thereby prevent neovascularization. Due to rather short (weeks) lifetime of these anti-VEGF molecules, such intravitreal injections need to be performed on a monthly basis. If successful, such treatments can maintain the visual acuity on a functional level until atrophic form of AMD ensues.

1.39.2.2.2 Retinitis Pigmentosa

Retinitis pigmentosa (RP) is a broad class of a variety of genetic disorders which typically affects patients in their twenties or thirties, with an incidence rate of approximately 1:4000 (Haim, 2002). This inherited disease typically begins with a loss of rod photoreceptors in the periphery, followed by a loss of the remaining cone photoreceptors in the central retina. As the disease progresses, patients start suffering from tunnel vision, with some baer light perception in the periphery, and central light sensitivity can eventually disappear as well. Retinitis pigmentosa is a prime candidate for gene therapy, and several clinical trials are being conducted today. However, due to the large variability in genetic defects that can lead to this condition, it is unlikely that one single cure for all its forms can be found.

The majority of RP patients retain some degree of sight (Grover et al., 1999), and hence only the patients with acuity significantly lower than that provided by the retinal implants can be considered candidates for prosthetic vision.

1.39.2.2.3 Blindness and Visual Acuity

Both retinitis pigmentosa and age-related macular degeneration are characterized by a significant loss in *visual acuity* – one of the most important characteristics of the visual function, which quantifies spatial resolution. Typically, it is measured by assessing the patient's ability to discriminate between objects on standardized charts. In the United States, visual acuity is most commonly measured in units of $20/x$, which means that one sees from 20 feet away an object equally well as a person with normal visual acuity would x feet away. A visual acuity of 20/10 is therefore twice better than normal, and a visual acuity of 20/40 twice worse than normal. People with a visual acuity of less than 20/200 are considered legally blind in the United States, while the World Health Organization sets the limit at 20/400. In countries with the metric system, the distance is expressed in meters, and since 20 feet is about 6 m, the units of visual acuity are $6/x$. The normal visual acuity (20/20) corresponds to the ability to resolve lines 1.75 mm apart from a distance of 20 feet, which corresponds to a visual angle of 1 min of arc, or 5 μm on the retina. Another common unit of visual acuity is LogMAR (for LOGarithm of the Minimum Angle of Resolution), defined as the negative decadic logarithm of the fractional visual acuity, so that the logMAR acuity is $-\log(20/x) = \log(x/20)$.

Visual acuity is a perceptual notion and reporting it in units of $20/x$ implies perceptual equivalence between what two subjects see. However, since the percepts elicited by visual prostheses are inherently very different from natural vision, it would be misleading to imply such equivalence. Therefore, it is important to keep in mind that even though spatial resolution of prosthetic vision is assessed in these units, these numbers reflect only spatial frequencies resolvable by the implanted patient, and not many other aspects of the visual function, such as contrast, dynamic range, shape distortions, etc.

1.39.2.2.4 Blindness and Visual Field

Importantly, the definition of legal blindness in the United States includes not only visual acuity below 20/200, but also a visual field under 20 degrees in the better seeing eye. To restore functional vision for patients blinded by RP, retinal implants should therefore aim at providing a sufficiently large field of view for comfortable orientation and ambulation, ideally exceeding 20 degrees. In AMD patients, however, central scotoma rarely exceeds 10–15 degrees of the visual field, and hence ambulation is not a problem. Therefore, in AMD patients with geographic atrophy, the implant should cover about 10 degrees in the middle of the scotoma and avoid damage to the adjacent healthy retina.

1.39.2.2.5 Animal Models of Retinal Degeneration

To study degradation of sight associated with retinal degeneration, as well as restoration of vision, researchers have developed a number of animal models of retinal degeneration (Marc et al., 2003). Retinal degenerations can naturally occur in a number of species, for example mice, rats and dogs. In addition, various transgenic mice, rats and pigs, as well as knock-out mice, are also commonly used to study visual impairment. Out of these, rodent animal models are generally the most cost-effective means of carrying out animal studies.

The relevance of rodent animal models for studying visual function is under debate. For example, humans and macaques share many features in their visual systems, such as foveated trichromatic vision, well-segregated parallel pathways in the visual thalamus, ocular dominance and orientation columns in the visual cortex (Nassi and Callaway, 2009). Rodents do not exhibit such similarity to the human visual system, but they do have an oculomotor reflex, and are capable of complex visual tasks, such as orientation discrimination (Huberman and Niell, 2011), and invariant object recognition (Zoccolan, 2015).

A well-established rat model of retinal degeneration is the Royal College of Surgeon (RCS) rat (Strauss et al., 1998). In these animals, a mutation in the receptor tyrosine kinase gene, *Mertk*, causes failure of the RPE cells to phagocytose shed photoreceptor outer segments, which leads to a build-up of cellular debris in the subretinal space. This, in turn, causes the progressive death of photoreceptors over a few months. By the age of 90 days (p90), the vast majority of photoreceptor outer segments are gone, while the inner nuclear layer and ganglion cells remain well preserved (**Fig. 1**C). Since RCS animals are born normally-sighted, they develop a normal visual cortex. This, combined with the relatively rapid progression of retinal degeneration – on the order of 3 months – makes them an attractive animal model for both *in-vivo* and *ex-vivo* studies of restoration of sight (Mandel et al., 2013).

The P23h and s344-ter are alternative rat models of retinal degenerations. In the P23h rat, both cones and rods degenerate as a result of a mutation in a rod-specific protein (Shen et al., 2005). It takes about 300 days post-natal for scotopic (rod-dominated) vision to disappear in P23h rats, and photopic (cone-dominated) vision remains present past 450 days. The slow onset of degeneration in these animals makes it difficult to obtain tissue with completely absent photoreceptors, making them less suitable for prosthetic studies.

There are over fifteen mouse models of retinal degeneration (Chang et al., 2002), with degeneration speeds ranging from a few days (*rd1*) to several months (*rd8* or *rd9* mice). Various models of retinal degeneration exhibit different functional properties as the disease advances, and it is unclear which of them correspond to human conditions. For example, in the rd1 mouse, both ON and OFF RGCs exhibit hyperactivity, while in the P23h rat, only OFF cells become hyperactive in the disease (Sekirnjak et al., 2011). A potential drawback of mice for retinal prosthetic studies is their small eye, which makes *in-vivo* studies very difficult.

A convenient alternative to genetic models of blindness is to cause a chronic detachment of the photoreceptors from the pigment epithelium, and thereby trigger a local retinal degeneration. This can be done, for example, by chronically introducing a subretinal implant in healthy animals (Mandel et al., 2013; Pardue et al., 2001; Lorach et al., 2015a), resulting in degeneration of photoreceptors above the implant in a few weeks. Retinal photocoagulation with a scanning laser can create a local ablation of the RPE combined with direct thermal damage to photoreceptors. As a result, outer retina atrophies in the damaged regions, which can be several millimeters in width, while the INL and ganglion cell layers are preserved (Lorach et al., 2015a). Selective ablation of

only the RPE cells using microsecond pulses is insufficient to trigger local degeneration, since RPE cells from adjacent healthy areas rapidly migrate into the damage zone (Lorach et al., 2015a). Both methods allow creating local retinal degeneration in otherwise healthy animals and could be useful for studying the interactions between prosthetic and normal vision, as would be the case in AMD patients.

1.39.2.2.6 Effects of Retinal Degeneration on the Neural Network

While retinal degenerations leave the inner nuclear layer and ganglion cells relatively intact for extended period of time (Humayun et al., 1999), significant changes in retinal organization can take place at the end phases of the disease, when the vast majority of the photoreceptors are lost (Marc et al., 2003; Marc and Jones, 2003; Jones and Marc, 2005). These changes are broadly called *retinal remodeling*. During this process, amacrine and bipolar cells can migrate either to the distal retina or to the ganglion cell layer. While all neurons appear to retain their normal basic molecular signatures, new synaptic connections are abundant. In the final stages of retinal remodeling, neuronal death can significantly deplete the inner nuclear and ganglion cell layers, with glial cells partially filling the space left by deceased neurons (Marc et al., 2003; Marc and Jones, 2003).

Electrical stimulation thresholds of certain sub-populations of the retinal ganglion cells in degenerate retina are higher than in the healthy one (Cho et al., 2016), while for others they do not change. Spontaneous RGC firing patterns change significantly with degeneration (Sekirnjak et al., 2011; Margolis et al., 2008; Menzler and Zeck, 2011). Hyperactivity has been reported in many rodent animal models of retinal degeneration, including asynchronous rhythmic activation of RGCs at 7–10 Hz frequencies in the rd1 mouse retina (Menzler and Zeck, 2011). In the rd10 mouse, RGCs types with normal electrical stimulation thresholds exhibit periodic bursting (Cho et al., 2016).

AMD patients are less likely to suffer from extensive retinal remodeling than RP patients since (1) the onset of the disease is much later in life and hence its duration is shorter, and (2) the peripheral retina is preserved, which helps maintaining more normal neural activity in the center via lateral connectivity in the retinal network. However, even in local retinal degeneration, spiking rate increases significantly (Tochitsky et al., 2014).

1.39.2.3 Electrical Stimulation of Neurons

Neural activity can be affected by modulating the cell potential using electric current, which can be delivered intra- or extracellularly. Changes in the *trans*-membrane voltage affect conductivity of the voltage-sensitive ion channels, which control the ion flux across the cell membrane. Typically, depolarization (decrease of *trans*-membrane voltage) leads to an increased influx of cations (Sodium in ganglion cells, Calcium in bipolar cells). This, in turn, leads to further opening of the sodium channels, which accelerates the charge intake. When the membrane potential exceeds a certain threshold, an action potential occurs in spiking neurons. Within about a ms, the action potential ends when the sodium channels are inactivated (closed) and the slower potassium channels open up, leading to an outflux of K^+ ions that lowers the membrane potential back to its resting value. Ion pumps then restore normal ion concentrations within a few ms (Malmivuo and Plonsey, 1995a). Modeling these processes requires solving Hodgkin-Huxley equations describing the dynamics of the voltage-sensitive ion channels on the cell membrane (Malmivuo and Plonsey, 1995b).

1.39.2.3.1 Intracellular Stimulation

Intra-cellular electrical stimulation is relatively well understood and widely used in laboratory settings for characterizing the electrical properties of cells. A simplified phenomenological model for intracellular stimulation, described by the Lapicque equation is computationally simple and closely matches the experimental measurements (Bostock, 1983; McIntyre and Grill, 1998).

In a resting state, the intracellular potential of a neuron is maintained by a number of mechanisms at approximately −70 mV, compared to the extracellular medium. A positive inflow of ions through sodium and leakage channels is compensated by an outflow of ions through potassium channels, and ion pumps balance the diffusion by actively moving ions across the cell membrane. Intracellular stimulation operates by injecting a current (I_s) into the target cell, for example by means of a fine-tip pipette. Modeling the neuron as a RC circuit, where the capacitor represents the capacitance of the cell membrane (C) and the resistor (R) limits the current of the active ion pumps, which maintain the cell membrane potential (**Fig. 2**A), leads to the following set of equations, which describes the electrical behavior of the cell:

$$\begin{cases} I_s = I_r + I_c \\ I_r = \dfrac{V - V_r}{R} \\ I_c = C\dfrac{\mathrm{d}V}{\mathrm{dt}} \end{cases} \tag{1}$$

From these equations we can derive the minimum current I_{th} to be injected into the cell over a duration τ to bring the membrane potential to a value V_{Th}:

$$I_{th} = \frac{(V_{Th} - V_R)/R}{1 - e^{-\tau/RC}} \tag{2}$$

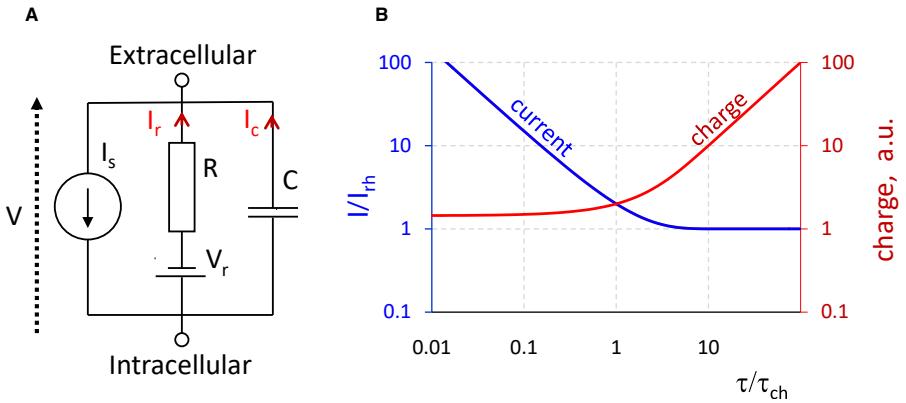

Figure 2 **Lapicque Model of a Neuron for Intracellular Stimulation.** (A) Equivalent circuit, including the membrane resistance *R*, capacitance *C*, battery maintaining the resting potential V_r, and the source of current (stimulus) I_s, which flowing through the resistor (I_r) and capacitor (I_c). (B) The resulting strength-duration relationship for intracellular stimulation, where stimulation current, *I* is presented in units of rheobase I_{rh}, and pulse duration τ - in the units of chronaxie τ_{ch}. Injected charge ($q = I.\tau$) is plotted in arbitrary units, shown on the scale on the right.

where V_R is the resting potential. If we define the *rheobase* current $I_{rh} = (V_{Th} - V_R)/R$ and the chronaxie time $\tau_{ch} = RC/\ln(2)$, this equation becomes:

$$I_{th} = \frac{I_{rh}}{1 - 2^{-\tau/\tau_{ch}}} \tag{3}$$

knownas the Lapicque equation, after the French scientist who first carried out this derivation in 1907.

If V_{th} is the threshold change of the membrane potential that elicits an action potential, this function, commonly known as the strength-duration relationship, defines the minimum current to be injected into a cell over a duration τ to elicit an action potential (Fig. 2B). Its asymptotic value at long pulse durations is called rheobase, while its time constant τ_{ch}, called the chronaxie, is defined as the duration at which the threshold current is twice the amplitude of the rheobase. On the short end of this curve, the threshold current scales as $I_{th} \propto 1/\tau$ and hence the charge of the pulse $q = I \cdot \tau$ is conserved (Fig. 2B).

More accurate description of the cellular activation should take into account the voltage-dependent conductivity and dynamics of the ion channels, which are described by the Hodgkin-Huxley equations (Malmivuo and Plonsey, 1995b).

1.39.2.3.2 Extracellular Stimulation

Extracellular electrical stimulation is the mechanism by which all clinical neural implants operate today. It works by polarizing cells in an electric field, instead of directly injecting current into the cell. The cell membrane is highly resistive, while its cytoplasm is very conductive. Therefore, when an electric field is applied across a cell in the extracellular medium, charges redistribute along the cell membrane and the cytoplasm rapidly becomes equipotential (within tens of ns) (Boinagrov et al., 2010). As a result, the *trans*-membrane potential step increases (i.e., the membrane becomes hyperpolarized) on the side of the cell facing the anode and decreases (the membrane becomes depolarized) on the opposite side. On the depolarized side of the membrane, the voltage-gated cation channels open, increasing the influx of positive ions (Sodium in ganglion cells, Calcium in bipolar cells), resulting in cellular depolarization as a whole. When the membrane potential exceeds a certain threshold, an action potential occurs in spiking neurons.

Extracellular electrical stimulation only depolarizes the cathode-facing section of the cell membrane. Therefore, it can only recruit a fraction of all the ion channels present on the cell membrane, and therefore it requires stronger stimuli to elicit responses than would be with uniform depolarization of the whole cell membrane in intracellular stimulation. Typically, at least ten mV must be applied across a cell soma to elicit a response, while a few mV would suffice for intracellular stimulation (Boinagrov et al., 2010).

If an action potential occurs during the stimulation pulse, the threshold current does not depend on pulse duration. This regime of stimulation is the rheobase (Fig. 3). When the stimulus ends before the action potential is generated, the influx of sodium ions during the stimulus may still be sufficient to put the neuron on the path of generating an action potential. For this, the sodium influx during the stimulus should exceed the stimulation threshold. The shorter the pulse, the stronger the stimulus needs to be in order to open enough ion channels and allow sufficient charge influx to exceed the stimulation threshold. This mechanism defines the rising part of the strength-duration dependence of the stimulation threshold with decreasing pulse duration (Boinagrov et al., 2010). The kinetics of different ion channels can vary significantly, and therefore the strength-duration dependence of the stimulation threshold varies for different cell types.

For intracellular stimulation, the threshold can be approximated as the charge required to depolarize the cell by a certain voltage, and therefore the threshold current scales inversely to pulse duration in this regime (Malmivuo and Plonsey, 1995b). In extracellular stimulation, however, the dynamics of the charge influx is more complex, and the strength-duration curve deviates from such a simple shape (Boinagrov et al., 2010). Since Na ion channels are faster than Ca ones, chronaxie in ganglion cells is shorter

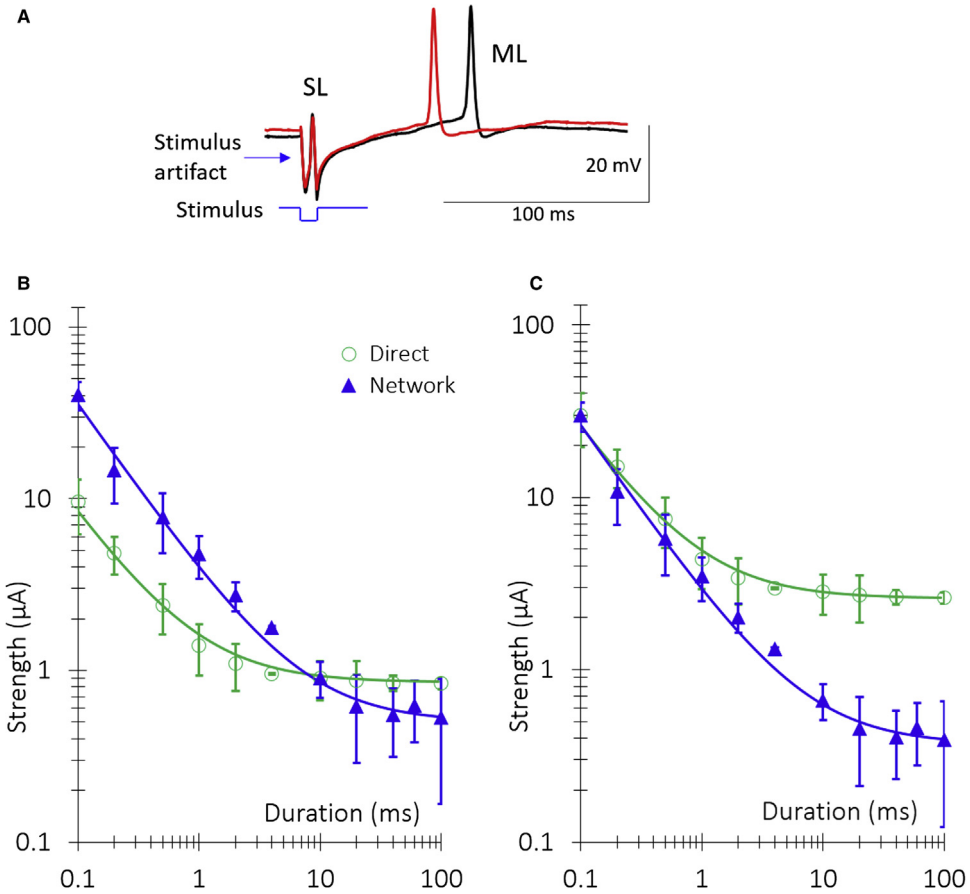

Figure 3 **Retinal Responses to Electrical Stimulation.** (A) RGCs respond to electrical activation of the retina with a combination of short latency (SL), medium latency (ML) and long latency (LL) action potentials. SL responses come from the direct activation of the RGCs, while ML responses originate in the inner nuclear layer (INL). LL responses likely originate in the photoreceptor layer (not shown here). (B) Strength-duration relationship for a stimulating electrode placed epiretinal and delivering cathodic-first current pulses. With short (<2 ms) pulses, stimulation threshold for direct activation of RGCs is lower than the network-mediated response, while long (>10 ms) pulses first activate the INL. (C) Strength-duration relationship for a stimulating electrode placed in the outer plexiform layer and delivering anodic-first current pulses. Long (10 ms) anodic pulses can activate the INL without directly eliciting activity in the GCL. Data adapted from Boinagrov et al. (2014).

than in bipolar cells (Fig. 3B and C), which provides an opportunity for selective stimulation of various cell types, as described in the next sections.

1.39.2.3.3 Upper Stimulation Threshold

It is widely assumed that the upper limit to somatic stimulation is the cellular or electrode damage threshold. However, it turns out that there is an upper stimulation threshold, above which no action potential can be elicited, and it is below the threshold of cellular damage. The upper stimulation threshold was observed in the retinal ganglion cells (RGCs) at pulse durations ranging from 5 to 500 μs. The ratio of the upper to lower stimulation thresholds varied typically from 1.7 to 7.6, depending on pulse duration (Boinagrov et al., 2012).

Computational modeling of extracellular RGC stimulation explained (and actually predicted) the upper limit by sodium current reversal on the depolarized side of the cell membrane (Boinagrov et al., 2010). According to the model, the upper threshold of stimulation is caused by reversal of the sodium ion current at strong depolarizations. For the sodium inflow, the current density is defined as $jNa \propto gNa \cdot (ENa - V)$, where g_{Na} is sodium channel conductivity, E_{Na} is the sodium Nernst potential (typically in the range of 35–50 mV), and V is the local transmembrane voltage. During the stimulus, the sodium ion channels are activated at the depolarized part of the cell membrane, increasing g_{Na} and j_{Na} and thus letting the positive sodium current into the cell, which may trigger the AP. At high stimuli, when V approaches E_{Na}, the term approaches zero and reduces the sodium inflow, j_{Na}. Upper threshold occurs when the total sodium inflow into the cell is insufficient for generating the AP. At higher stimuli, when V exceeds E_{Na}, j_{Na} becomes negative, so Na ions flow out of the cell through the open ion channels, and no AP is generated. Similar effect can occur with bipolar cells, when the voltage-gated Ca channels in their axonal terminals experience *trans*-membrane voltage exceeding their Nernst potential (Werginz and Rattay, 2016).

1.39.2.3.4 Role of Electrode Placement and Pulse Polarity

Since the distribution of ion channels over neurons is rarely isotropic, orientation of the electric field significantly affects the stimulation threshold. It is lower when the side of the cell with the highest concentration of the responding ion channels (Na for ganglion cells, Ca for bipolar) is depolarized. Therefore, placement of the stimulating electrode (above or below the retina - epiretinal or subretinal) as well as pulse polarity (anodic or cathodic) affects the stimulation thresholds.

Dependence of the stimulation threshold on pulse polarity has been confirmed many times experimentally. For epiretinal stimulation of RGCs, cathodic-first pulses have a lower stimulation threshold (Jensen et al., 2005; Fried et al., 2006; Boinagrov et al., 2014) due to the higher concentration of Na channels over the region of RGCs facing the inner limiting membrane, near the axonal hillock (Fried et al., 2006). For subretinal stimulation of RGCs, anodic-first pulses have lower stimulation thresholds for the same reason (Boinagrov et al., 2014; Jensen and Rizzo, 2006). Similarly, for subretinal stimulation of the inner nuclear layer, anodic pulses have lower threshold (Boinagrov et al., 2014) because bipolar cells have a higher concentration of Ca ion channels in their axonal terminals (Werginz et al., 2015). For small electrodes, proximity to the target neuron is another factor that significantly affects the stimulation thresholds, since in this case the electric field rapidly decreases with distance. A combination of good electrode placement and proper choice of the stimulation pulse parameters can help achieve selective activation of the various retinal layers (Boinagrov et al., 2014).

Generally, RGC responses to electrical stimulation can be classified into three categories, depending on their origin. *Short Latency* (<2 ms) RGC responses correspond to action potentials elicited directly in the ganglion cells (**Fig. 3**A). *Medium Latency* responses (typically on the order of 3–50 ms) are mediated by stimulation of the inner nuclear layer. Electrical stimulation of the photoreceptors, or possibly amacrine cell-mediated activation of the retina, accounts for the *Long Latency* responses (not shown in **Fig. 3**A). Selectivity of stimulation quantifies the ability to activate one layer of cells without affecting the others, and is defined as the inverse ratio of the stimulation thresholds of the layer of interest vs. other layers.

Epiretinal prostheses aim at eliciting RGC responses through direct stimulation, so selectivity for this approach is the threshold for medium latency action potentials divided by the threshold for short latency action potentials. Measurements of the strength-duration relationships of direct and network-mediated responses (Boinagrov et al., 2014) demonstrated that short (<1 ms) epiretinal cathodic-first pulses coming from an epiretinal electrode provide a best selectivity of 3 (**Fig. 3**B).

For subretinal prostheses, selectivity is the ratio of short latency thresholds over medium latency threshold, as subretinal implants generally target cells in the inner nuclear layer. Long (>4 ms) anodic-first pulses in the outer plexiform layer (i.e., in a subretinal position) provide the best selectivity, exceeding a factor of 6 for 20 ms pulses (Boinagrov et al., 2014) (**Fig. 3**C).

Relative positioning of the active and return electrodes in the implant affects the cross-talk between neighboring pixels, and thereby can also affect selectivity, contrast and attainable resolution (Palanker et al., 2005; Loudin et al., 2007; Flores et al., 2016). Many implants operate with a common remote return electrode, in the so-called monopolar configuration. Cross-talk between neighboring pixels becomes more pronounced with a higher number of simultaneously activated electrodes. To circumvent this limitation, arrays in which each stimulating electrode is surrounded by a local return electrode have been developed (Loudin et al., 2007; Mathieson et al., 2012). A drawback of using local returns is that they decrease the penetration depth of the electric field, compared to a monopolar configuration with same pixel size, which imposes more stringent requirements on proximity between the stimulating electrodes and target cells. This has led to the development of 3-dimensional implants described below.

1.39.2.3.5 Axonal Simulation

In cell somas, membrane polarization is defined by the voltage step across the cell boundaries, i.e., by the integral of electric field along the cell. However, the axons are considered to be too thin (<1 μm) to accumulate a significant voltage step across them. Axons are modeled as leaky cables, where activation function is defined by the derivative of electric field along the axon (Malmivuo and Plonsey, 1995c), which determines the misbalance of the current entering and leaving the axon through its membrane. Therefore, uniform electric field should not produce axonal stimulation. This phenomenon enables some field shaping-based solutions to the problem of axonal stimulation.

For a point source, cathodal activation has about 5 times lower threshold than anodal. However, at sufficiently high cathodal stimuli, the central activation zone is surrounded by the inhibition zone, creating a so-called “anodal surround block”, which limits the dynamic range of cathodal stimulation.

1.39.3 Approaches to Retinal Prosthetics

1.39.3.1 Anatomical Placement of the Stimulating Electrodes

Depending on their location in the patient’s eye, retinal implants fall into one of three categories: epiretinal, subretinal or suprachoroidal. In the *epiretinal* approach, prostheses target primarily the retinal ganglion cells, using electrodes placed on top of the inner limiting membrane (**Fig. 1**C) (Ahuja et al., 2011; Humayun et al., 2012). Since the action potential is a binary response, modulating the stimulus amplitude above the threshold does not affect amplitude of the resulting spike, and hence natural modulation strategy for RGCs is by stimulation frequency. Epiretinal devices are less dependent on the health of the inner retina and can operate as long as the RGCs survive. However, abnormally high spontaneous firing rate of ganglion cells, frequently observed in

animal models of retinal degeneration, represents a problem since it impedes the ability of the implant to encode a desired sequence of spikes or diminishes the corresponding perception.

In *subretinal* approach, arrays of electrodes located between the inner nuclear layer and the pigment epithelium replace the degenerated photoreceptor layer and target primarily the surviving bipolar cells (**Fig. 1**C) (Zrenner et al., 2011; Lorach et al., 2015b). Subretinal implants deliver visual information to non-spiking inner retinal neurons, and stronger stimuli are encoded with higher amplitude or longer duration pulses. Output signals from bipolar cells are then transmitted to the ganglion cells via synaptic connections and converted into the action potential trains. In this approach, the goal is to maintain some of the signal processing properties of the retinal network, so that the spiking patterns elicited in the RGCs will resemble those arising under normal physiological conditions. However, changes in the retinal network during degeneration may significantly impact retinal signal processing, and therefore will likely influence our ability to encode visual information. Subretinal prostheses are particularly vulnerable in this regard, since they rely on connections between the inner retinal neurons and the ganglion cells.

Implanting a subretinal device involves creation of a local retinal detachment and a small retinal incision, through which the device is placed into the subretinal space, after which the retina is reattached. Excessively traumatic implantations can lead to fibrosis and scaring. In the case of wired subretinal implants, large areas of the retina need to be detached during implantation, which is a significant challenge with fragile diseased retinas. Explanting a subretinal device is significantly more difficult than epiretinal, although it has been done with the Alpha IMS implants (see Section "**The Alpha IMS/AMS Subretinal Implant**"**)**. Explaniability of the photovoltaic subretinal devices remains to be demonstrated.

In a third approach, called *suprachoroidal*, the implant is placed below the choroid into the sclera (**Fig. 1**C). While this approach has been deemed to be surgically less risky than both epi- and subretinal prostheses (Fujikado et al., 2011; Ayton et al., 2014), the larger distance between the stimulating electrodes and retinal neurons greatly restricts attainable spatial resolution. Therefore, such implants have large (~mm) electrodes and are placed in the periphery of the visual field, since they are designed to help with low-resolution peripheral vision, primarily for ambulation.

1.39.3.1.1 Three-Dimensional Interfaces

The unexpected discovery that retinal tissue robustly migrates into voids in the subretinal space suggested a possibility of improving proximity between the stimulating electrodes and target cells by making subretinal implants three dimensional, as opposed to planar arrays (Palanker et al., 2004) (**Fig. 4**). Structures with chambers and pillars were found to induce retinal migration, with voids in the subretinal space being filled within days after implantation (Butterwick et al., 2009; Ho et al., 2019; Flores et al., 2019). Cells in the inner nuclear layer easily migrate through apertures larger than 10 μm. With 10 μm-diameter pillars and

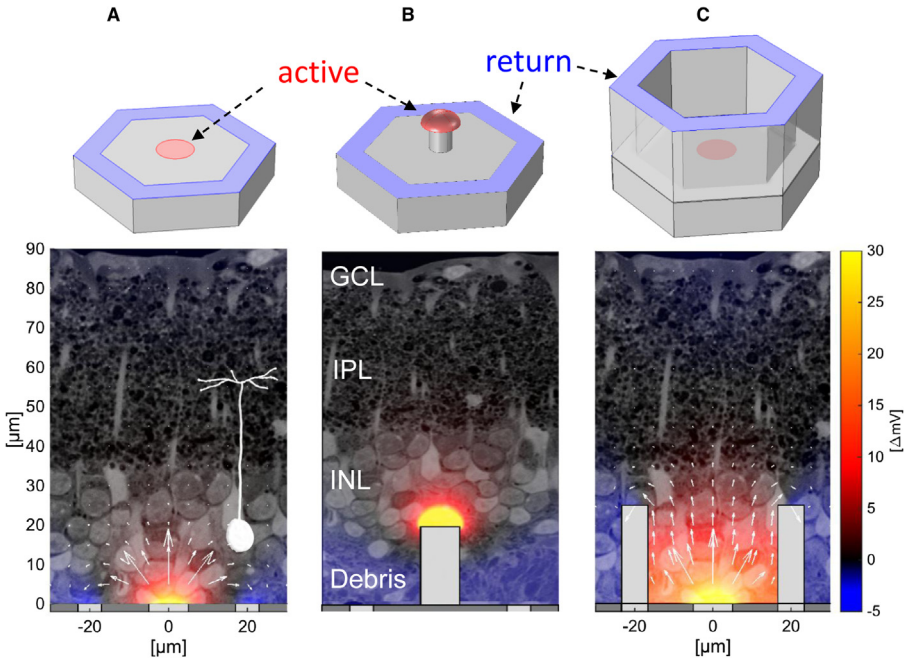

Figure 4 Retinal Migration into 3-D Implants. (A) As flat pixels become smaller, penetration of electric field (shown in false color) into the tissue becomes insufficient for stimulation of bipolar cells (shown in white on top of the retinal histology). (B) The inner retinal cells robustly migrate into the voids between pillars or walls in the subretinal space, within a few weeks post-implantation. This way, cells are brought closer to the top of the pillar electrodes. (C) With a return electrode on top of the honeycomb wells, electric field is aligned vertically, matching the orientation of bipolar cells. This way penetration depth is decoupled from the pixel width, which enables scaling the pixel size down to cellular dimensions at the same stimulation threshold.

40 μm center-to-center spacing, cells of the inner nuclear layer fill the space between pillars (Ho et al., 2019) (Fig. 4B). Similarly, cells migrate into the wells of 20 μm and larger, thereby enabling the honeycomb-shaped electro-neural interface (Flores et al., 2019) (Fig. 4C). In general, pillar implants appear to maintain a more natural topology of the various retinal layers than implants with wells, although it is unclear yet whether this has implications for retinal prostheses. Explanation of 3-dimensional structures is likely to be more difficult than that of the flat arrays. Discussion of this topic continues in the section "**Improving Proximity to the Target Neurons in Subretinal Space**".

1.39.3.2 Delivery of Information and Power to the Implant

Transfer of information and power to the implant is a challenging engineering problem, since direct connection of an implant to external electronics via transcutaneous wire is prone to infections and severe scarring (Knutson et al., 2002). Therefore, in modern implants, transmission of information and power to the implant is done wirelessly, using one of the following techniques: (1) delivery of power and serial telemetry of the data through inductive coils, (2) optical transmission of the data with power delivery through inductive coils, or (3) optical delivery of data and power to the implant.

1.39.3.2.1 Serial Telemetry of the Data

Inductive coils are widely used to transmit power and data to medical devices, including cochlear implants and retinal prostheses. In such systems, an AC current driven through an external transmitting coil induces an AC current in the implanted receiving coil, which is converted into DC current in the implant. Coupling efficiency between the coils is described by the coupling coefficient - the fraction of the magnetic flux produced by the current in the primary coil that links with the secondary coil. The transmitting and receiving coils in implanted systems are typically weakly coupled (Wang et al., 2005), with the coupling coefficient k in the range 0.08–0.24, much lower than in normal transformers, where $k \sim 0.9$.

A capacitor in series with the receiving coil creates a tuned resonance at the transmitter frequency f, and the resulting circuit amplifies the received voltage by a quality factor Q, typically in the range 10–100. Quality factor increases with frequency, however RF absorption in tissue increases exponentially beyond a few MHz (Osepchuck, 1983), limiting the range of useful frequencies to below a few MHz.

Unfortunately, while a high Q coil is efficient for receiving power, it is a rather poor data receiver, which makes it challenging to use a single coil for both data and power. According to the Shannon-Hartley theorem (Shannon, 1998), the data capacity C of a coil can be expressed as:

$$C = \frac{f}{Q}\log(1 + SNR) \tag{4}$$

where$C$ is in bits/s and f/Q is the bandwidth of the circuit, inversely proportional to the quality factor Q. SNR in this equation is the signal-to-noise ratio of the transmitted signal. For this reason, one coil is often used for power and another for data (Wang et al., 2005), with data transmitted at a higher frequency and with a lower quality factor coil. Efforts have been put toward developing single receiving coil systems with high Q, that can also efficiently deliver data, and one such system achieved transmission rates above 1 MB/s (Liu et al., 2000). In terms of data bandwidth requirements, the maximum number of pixels N that can be driven at a refresh rate R with S stimulation (gray) levels is then:

$$N = \frac{C}{R\log_2 S} \tag{5}$$

For example, a data rate of 1 MB/s can support $64 \times 64 = 4096$ pixels with a refresh rate of 60 Hz and 16 gray levels in the image.

Another option is transmission of power via RF link, by serial telemetry of the data via optical link from the goggles to receiver on the implant, as implemented in the IRIS II system (Pixium Vision, Paris, France) (Hornig et al., 2017). Since optical data transmission rate is at least one order of magnitude higher than with RF coils, much more information can be delivered to the implant.

Since visual information transmitted from the camera to the implant via serial telemetry does not depend on eye movements, this approach creates two problems. (1) The brain expects images to shift on the retina during eye movements. Since the stimulation patterns in such implants do not translate with the eye movement, the brain interprets this lack of retinal shift as motion of the object. Similar effects have been reported with cortical visual prostheses (Naumann, 2012). To avoid this phenomenon, patients are asked to keep their direction of gaze steady. (2) Instead of using natural eye scanning, patients are required to scan the visual field with their heads –a very unnatural paradigm. These limitations can be alleviated by incorporating an eye tracking system, which electronically shifts the image delivered to the implant according to the direction of gaze (Caspi et al., 2018).

It is difficult to scale coil-based designs to thousands of electrodes for two reasons: (1) doing so requires a very wide data bandwidth, (2) wiring of thousands of electrodes makes the cable quite rigid and the feed-through rather bulky. Multiplexing the signals on the array itself would reduce the required number of wires, but it adds electronics to the retinal array itself, which affects its heat dissipation, weight and flexibility.

A number of retinal implants use serial telemetry for data transmission: the Argus II (Second Sight Medical Systems, Sylmar, CA), shown in Fig. 5, suprachoroidal implant (Ayton et al., 2014), IRIS II (Hornig et al., 2017), the Boston Retinal Implant (Rizzo et al., 2011).

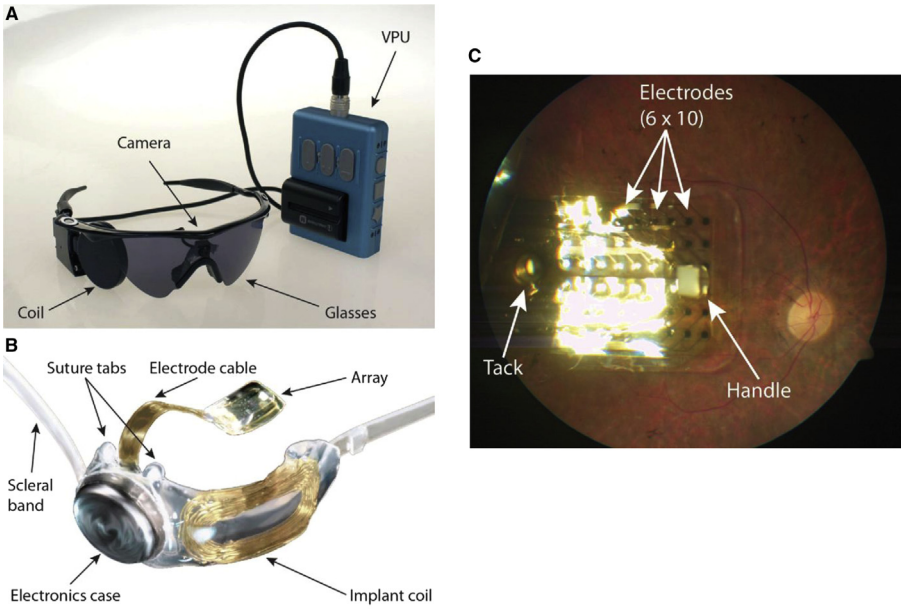

Figure 5 The Argus II Epiretinal Implant. (A) Photograph of the external portion of the Argus II prosthesis system, including glasses-mounted video camera, radio-frequency (RF) coil, and video processing unit (VPU) with rechargeable battery. **(B)** Photograph of the implantable portion of Argus II prosthesis system including the 6 × 10 electrode array, electronics case, and the implant RF coil. (C) Fundus photograph of an Argus II array implanted in the macular region. A retinal tack secures the electrode array to the sclera. The surgeon uses the white handle to position the device in the eye. Reprinted, with permission, from Humayun et al. (2012).

1.39.3.2.2 Powered Implants With Integrated Camera

A few designs have been proposed that deliver only power through inductive coupling and transmit visual information through the natural optics of the eye (Loudin et al., 2007; Zrenner et al., 2011; Ha et al., 2016; Iridium Medical Technologies). The best known of these systems was the Alpha IMS/AMS (Retina Implant AG, Reutlingen, Germany), shown in **Fig. 6**. Their subretinal implant was a camera with an active circuitry and stimulating electrode in each pixel that converts incident images into electrical stimulation patterns on the electrode array. It included a subdermal power receiving coil placed behind the ear, similarly to cochlear implants. Power was then routed to the subretinal implant via a *trans*-scleral cable (Stingl et al., 2017). This company has been dissolved in 2019.

Implants with integrated photosensitive pixels efficiently receive visual information, and they naturally couple eye movement to the stimulation pattern on the implant. However, the cable connecting the retinal implant to the extraocular power supply makes the implantation procedure difficult, long, and prone to complications. In the case of the Alpha IMS/AMS implant, developing a flexible and robust *trans*-scleral cable and feed-through that withstands the effects of eye movements over the long term remains a challenging engineering problem (Daschner et al., 2017).

1.39.3.2.3 Photovoltaic Systems

The third category of retinal implants receives both data and power by light, via the natural optics of the eyes (Mathieson et al., 2012; Ghezzi et al., 2013). These implants directly convert incident light into electric current to stimulate the nearby neurons. Using an array of photodiodes as a subretinal implant was first proposed in the 90s (Chow et al., 2004). In that design, the photovoltaic pixels in the implant were expected to convert ambient illumination into stimulating currents. However, ambient light on the retina is much too dim for photovoltaic stimulation (Palanker et al., 2005). In addition, photovoltaic conversion of continuous illumination cannot provide charge-balanced current pulses, which are required to avoid hydrolysis and electrode erosion.

A revised concept of a photovoltaic subretinal implant powered by intense pulsed light projected from video glasses was proposed in 2005 (Palanker et al., 2005), first implemented in 2007 (Loudin et al., 2007), and has been actively developed since then (Mathieson et al., 2012; Lorach et al., 2015b). Intense illumination can be provided by a near-the-eye display (Goetz et al., 2013), similar to augmented-reality glasses, apart from its significantly higher irradiance. A pocket computer provides a convenient means of processing images prior to displaying them onto the implant (**Fig. 7**). In order to avoid photophobic and phototoxic effects of bright illumination, photodiode-based systems can use near-infrared (850–915 nm) wavelengths, invisible to the remaining photoreceptors.

The photocurrent created by the implant increases linearly with light intensity, until saturation is reached at a level defined by the ratio of the maximum photo voltage to the tissue impedance. Adding photodiodes in series helps increasing this maximum voltage, but pixels then require more light since the incident illumination is divided between the photodiodes in each pixel

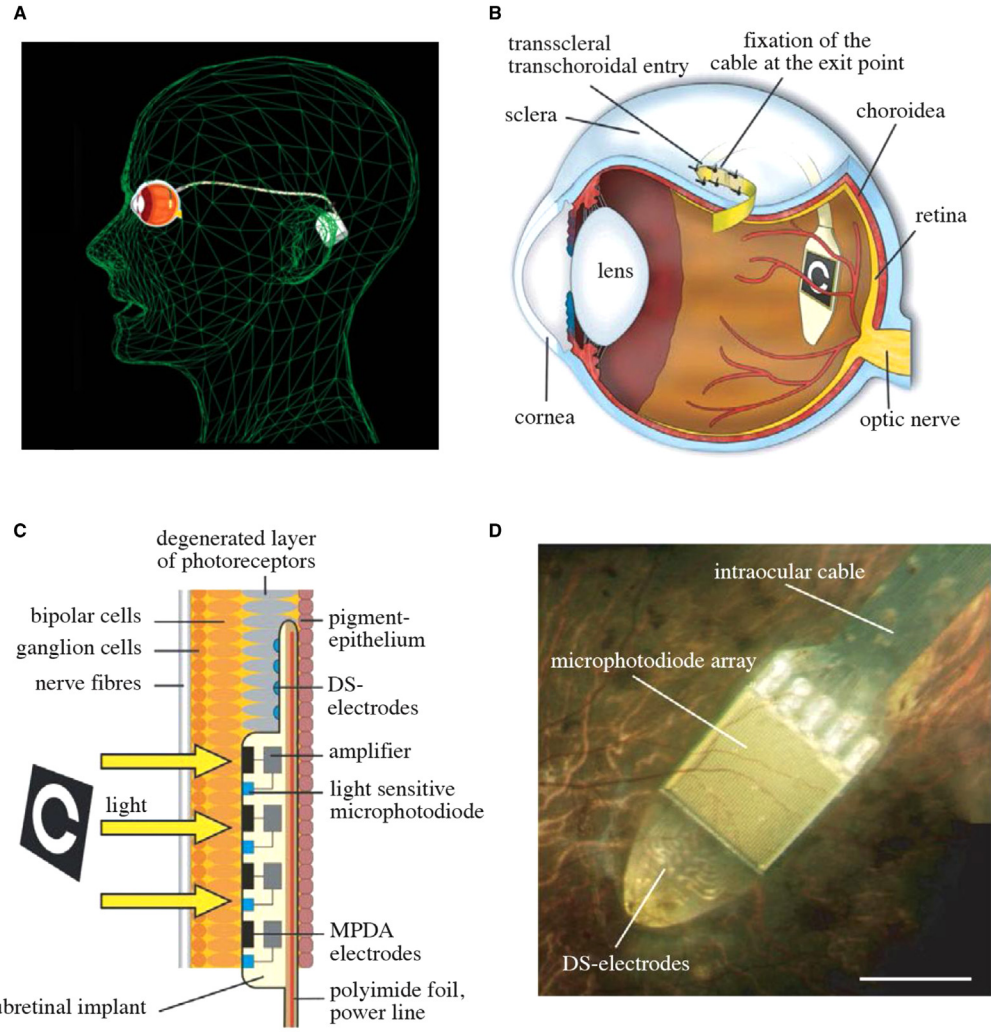

Figure 6 **The Alpha IMS Subretinal Implant.** **(A)** The cable from the implanted chip in the eye leads through the sclera, under the temporal muscle to RF receiver behind the ear. **(B)** Implant under the transparent retina, with the power cable exiting the eye 3 mm behind the limbus. **(C)** Subretinal camera with photodiodes, amplifiers and electrodes in relation to retinal neurons and pigment epithelium. **(D)** View of the tip of subretinal implant at the posterior pole through a patient's pupil. Scale bar: 3 mm, corresponding to 10° visual angle. Reprinted, with permission, from Zrenner et al. (2011).

(Boinagrov et al., 2016). Instead of a crystalline silicon, photovoltaic elements based on light-sensitive polymer films have also been proposed (Ghezzi et al., 2013).

An attractive feature of photovoltaic systems is that they do not require any wires (Mathieson et al., 2012; Lorach et al., 2015b). Therefore, an implant can consist of a large number of independent modules that tile the visual field. These modules can be inserted into the subretinal space via a small incision and follow the curvature of the eye, making the surgery minimally-traumatic (Lee et al., 2016).

1.39.3.3 Safety Considerations

1.39.3.3.1 Thermal Limits

For both RF- and optically-powered implants, tissue heating resulting from absorption of electromagnetic radiation and energy dissipation in the implanted electronics must be kept within acceptable safety limits. The ISO norm 14708-1 article 17.2 specifies that temperature rise in chronic operation should not exceed 2 °C, since this is within the natural range of body temperature variation. The heating induced by the implant is governed by the following equation (Sramek et al., 2009), which can be solved numerically using finite element models:

$$\rho c_p \frac{\partial T}{\partial t} = \nabla(k\nabla T) + Q(\boldsymbol{x}, t) - A_p(\boldsymbol{x})\rho_b c_b (T - T_o) \tag{6}$$

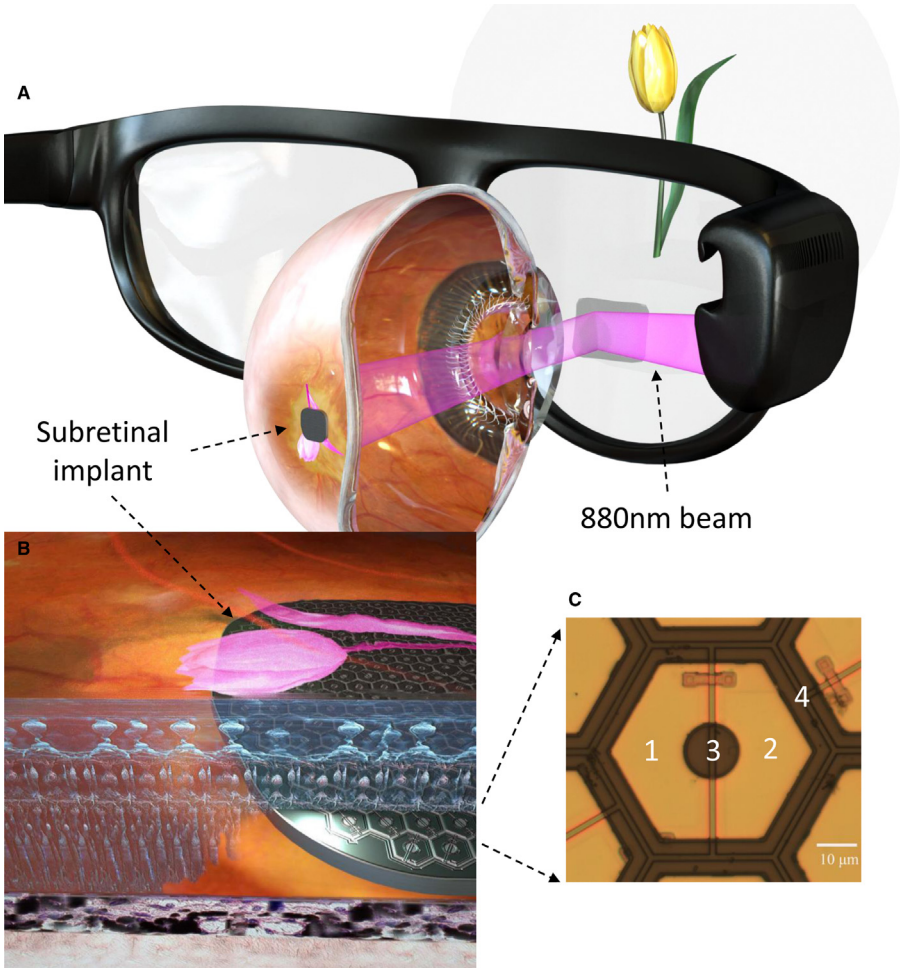

Figure 7 **Subretinal Photovoltaic Implant (PRIMA).** (A) Camera in augmented-reality glasses captures visual scenes, which are processed by a mobile computer. Images are then projected into the eye using pulsed near infrared (880 nm) light. (B) The 30 μm thick subretinal implant is composed of photovoltaic pixels which convert incoming light into electric current to stimulate the nearby inner retinal neurons. (C) Close-up of a 55 μm-wide pixel, which includes two diodes (1 and 2) connected in series between the active (3) and return (4) electrodes. Scale bar: 10 μm.

where ρ and c_p are the density and heat capacity of the medium, k is the thermal conductivity, Q is the volumetric heat source term, A_p is the local blood perfusion rate, ρ_b and c_b are the density and heat capacity of the blood, and T_0 is the arterial temperature, often assumed to be the same as the baseline body temperature, 37 °C.

For optical implants, the use of bright illumination is a safety concern. Visible and near-infrared (below ~900 nm) illumination is absorbed primarily by pigmented tissues, such as the retinal pigment epithelium, with a practically negligible absorption ($<0.06\ \mathrm{cm}^{-1}$) in transparent ocular layers such as the cornea, lens, and neural retina. Ocular safety standards (Delori et al., 2007) provide some guidelines as to the maximum permissible radiant power ($MP\varphi$) that may be chronically delivered to the retina:

$$MP\varphi = 6.93\$10^{-5}\Lambda\Xi P^{-1} \tag{7}$$

where $\Lambda = 10^{0.002(\lambda\ -\ 700)}$ in the 700–1050 nm range, with $\Lambda = 2.5$ at $\lambda = 905$ nm. The parameter Ξ depends on the angular spread of the incident beam, and for retinal spot sizes greater than 1.7 mm in diameter is 29.3 W/mm^2. Parameter P is the pupil factor which accounts for pupil constriction or dilation, and is exactly 1 for infrared wavelengths in the absence of dilating drugs. For a 905 nm wavelength, the average irradiance limit is therefore 5.2 mW/mm^2. It is important to emphasize that temperature increases with increasing spot size, which this standard does not take it into account.

For single-pulse exposure, the peak irradiance limit in the 0.05–70 ms duration range is described by (Delori et al., 2007)

$$MP\varphi = 6.93\$10^{-4}\Lambda C_T \Xi C_E t^{-0.25} \tag{8}$$

At 905 nm, $MP\varphi\ = 285t^{-0.25}$, where t is in ms and the result is in mW/mm^2. For example, the peak irradiance limits are 285, 202 and 160 mW/mm^2 for 1, 4 and 10 ms pulses, respectively.

Detailed studies of retinal heating with and without the implants under various illumination settings have shown that under typical use conditions, the temperature increase associated with activation of a subretinal photovoltaic implant is not expected to exceed 0.5 °C, well within the safety limits for chronic use (Lorach et al., 2016).

1.39.3.3.2 Electroporation

Electrical stimulation of neural tissue has the potential to cause irreversible cellular damage (Mccreery et al., 1990). One process by which damage occurs is called electroporation. Strong electric field can produce sufficiently high *trans*-membrane voltage (~1 V) to make penetration of water into the hydrophobic lipid bilayer energetically favorable, which leads to formation of nanometer-scale pores in the cell membrane (Neumann, 1992). The damage threshold current density j scales inversely with the square root of pulse duration ($j \sim t^{-0.5}$) (**Fig. 8**A) (Butterwick et al., 2007). Since on the short end of the pulse durations, stimulation threshold scales as 1/t, and on the long end it is flat (rheobase), the ratio of the electroporation threshold to stimulation threshold reaches its maximum at pulse duration approximately equal to chronaxie. On both sides of this peak, the ratio decreases toward shorter and longer pulses as $t^{0.5}$ or $t^{-0.5}$, respectively (**Fig. 8**B).

With large electrodes, retinal stimulation thresholds (Jensen et al., 2003) are approximately two orders of magnitude below the electroporation thresholds (Butterwick et al., 2007), leaving a sufficiently wide window for safe stimulation of the retina. Within two orders of magnitude of pulse duration above and below the chronaxie ($0.01t_{ch}$; $100t_{ch}$), this ratio decreases to one order of magnitude (**Fig. 8**B).

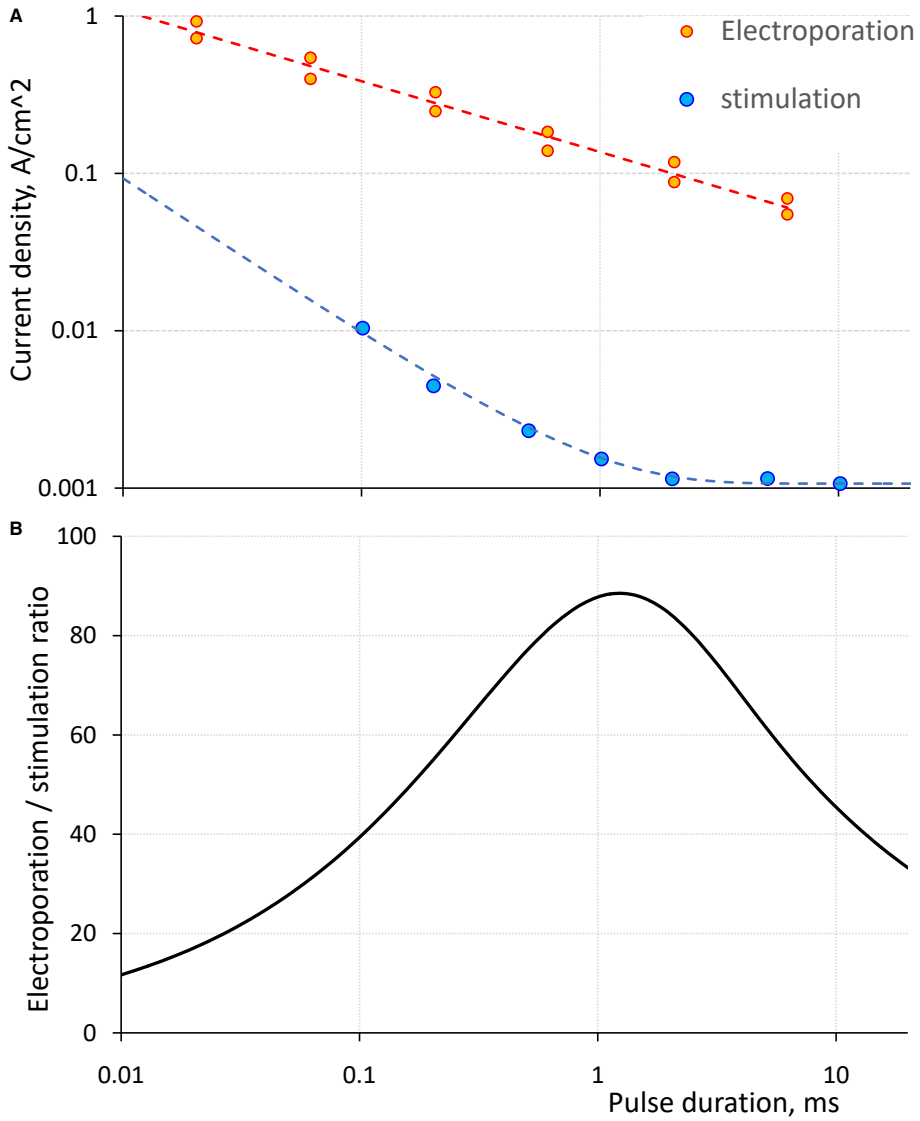

Figure 8 **Retinal Electroporation and Stimulation Thresholds Measured with Large Electrodes.** (A) Retinal electroporation threshold and stimulation threshold as a function of pulse duration, measured with large (0.5–1 mm) electrodes. (B) Ratio of the damage threshold to the stimulation threshold. Adapted from Butterwick et al. (2007).

1.39.3.3.3 Electrochemical Limits

In addition to cellular hyperthermia and electroporation, cellular damage can also be caused by the leaching of toxic electrode materials into the medium, or by local changes in pH. Neural stimulation electrodes have been extensively studied in recent years, and a large body of literature is available on the topic (Merrill et al., 2005; Robblee and Rose, 1990; Cogan, 2008). Electrochemical safety limits vary with the electrode material and with mechanisms of charge injection, which are either capacitive or faradaic (Cogan, 2008). For both mechanisms, stimulation pulses need to be charge-balanced and within the safe limits of the electrode potential to avoid irreversible oxidation or reduction of the electrode material as well as other irreversible electrochemical reactions in the medium (Merrill et al., 2005; Robblee and Rose, 1990). Briefly, the most common harmful processes include electrolysis of water, with consequent gas formation and changes in pH, and metal dissolution due to the formation of soluble metal complexes (especially with Pt electrodes) (Cogan, 2008).

Capacitive electrodes are usually porous to provide a large surface area, and/or employ high dielectric constant materials, such as Titanium Nitride (Weiland et al., 2002). Faradaic charge-injection materials rely on reversible oxidation and reduction reactions to inject the current. These electrodes typically provide higher charge injection than capacitive interfaces, but care should be taken in selection of the stimulation waveforms to avoid irreversible processes. The most common materials for such electrodes include Platinum and Platinum Iridium alloys, as well as activated and sputtered Iridium oxide films. **Table 1** summarizes the charge injection limits of various electrode materials used in retinal prosthetics. Charge injection limits typically increase with pulse duration, especially for porous materials (not shown in **Table 1**).

1.39.3.3.4 Implant Encapsulation

Exposure of an implant to body fluids can lead to its erosion and eventual failure (Daschner et al., 2017). Implants can also trigger strong tissue reaction if they are not properly encapsulated in biocompatible materials. This tissue reaction may lead to formation of a glial or fibrotic seal around the implant, which will increase both the distance between the electrodes and target neurons and impedance of the stimulating electrodes (Butterwick et al., 2009). For these reasons, electronics in the majority of neural implants is enclosed in metallic or ceramic containers, with feed-through connectors to the power source and electrode array. The resulting implant hermetically isolated from the corrosive body fluids is stable, but bulky. Surgical procedures then involve placing different modules (coil, power and data-processing electronics as well as the electrode array) and routing interconnecting cables in the patient (Humayun et al., 2012; Zrenner et al., 2011).

While crystalline silicon implants are well tolerated over the short term (Pardue et al., 2001), detectable degradation occurs over a year (Lei et al., 2016). Such implants require a stable and biocompatible layer to provide protection against water and ion ingress. Dielectric materials deposited by low-pressure chemical vapor deposition at high temperatures (800–900 °C) have exhibited good stability *in-vivo* (Anderson et al., 1989; Weiland and Anderson, 2000), however the deposition temperatures are incompatible with the integrated circuits manufacturing processes. Polymers, such as Parylene, are used in the medical industry for encapsulation of neural implants (Loeb et al., 1977; Hsu et al., 2009), but Parylene absorbs water and develops cracks (Kane et al., 2013), and therefore cannot be used for encapsulation of unprotected integrated electronic circuits. Atomic layer deposited Al_2O_3 is conformal and hermetic, and as such can provide decent encapsulation. However, it slowly dissolves in water (Potts et al., 2011). Diamond-based coatings (Hadjinicolaou et al., 2012; Roy and Lee, 2007; Chen et al., 2014) and amorphous Silicon Carbide (Bolz et al., 1996) deposited at low temperatures are being explored as other possible encapsulating materials for neural implants. Recent studies have provided promising results regarding biocompatibility of diamond interfaces (Bendali et al., 2014). It remains to be seen, however, whether the limited charge injection capability of these interfaces is sufficient for safe and efficient retinal stimulation. Plasma-enhanced chemical vapor deposited amorphous silicon carbide (SiC) is a promising material for encapsulating neural implants, as SiC films do not dissolve in accelerated aging tests. Care should nonetheless be taken with SiC films deposited over steps and rough surfaces, as defect density then increases significantly. A combination of thermal Silicon Oxide coated with SiC could provide adequate protection of retinal implants (Lei et al., 2016).

1.39.4 Pre-clinical Evaluation of Prosthetic Vision

1.39.4.1 Retinal Response to Electrical Stimulation *Ex Vivo*

Epiretinal and subretinal implants share the common goal of encoding visual information in a degenerate retina. However, they rely on activation of distinct neural layers to elicit visual percepts. While the epiretinal approach focuses on stimulating the output cells

Table 1 Safe charge-injection limits of the electrode materials

Material	*Mechanism*	*Max. Q_{inj} (mC/cm^2)*	*Potential limits vs. Ag|AgCl (V)*
Pt, PtIr alloys	F, C	0.05–0.15	−0.6–0.8
AIROF	F	1–5	−0.6–0.8
SIROF	F	1–10	−0.6–0.8
TiN	C	~1	−0.9–0.9
PEDOT	F	15	−0.9–0.6

AIROF, Activated Iridium Oxide Film; SIROF, Sputtered Iridium Oxide Film; F, Faradaic; C, Capacitive.
Adapted from Cogan (2008).

of the retina - ganglion cells, the subretinal approach aims at eliciting activity in the inner nuclear layer (primarily bipolar cells) and relies on transmission of their responses to the ganglion cells via retinal neural network. As such, retinal response to epiretinal and subretinal stimulation differs greatly, and the encoding strategies for both types of implants should vary accordingly.

1.39.4.1.1 Epiretinal Stimulation

1.39.4.1.1.1 Stimulation Thresholds

Retinal ganglion cells are spiking neurons that encode visual information in the form of trains of action potentials. Epiretinal implants aim at directly eliciting the trains of action potentials in the RGCs, with each stimulation pulse encoding a single spike. A wide body of literature has studied the response of RGCs to direct activation with electrodes of various sizes (Humayun et al., 1994; Weiland et al., 2000; Sekirnjak et al., 2006). Typically, RGCs respond to direct activation with a single action potential elicited within 3 ms of the stimulation pulse, and latency of the response decreases with increasing stimulus strength (Boinagrov et al., 2014). When the retina is carefully pressed against epiretinal electrodes, action potentials can be elicited even within 1 ms of the stimulus (Jepson et al., 2013). The good temporal precision of direct RGC activation and short (sub-ms) stimuli enable multiplexed activation strategies, where only a few electrodes in an implant are activated at a time. This approach reduces cross-talk between neighboring electrodes and might be beneficial for achieving better spatial confinement of electric fields (Flores et al., 2016).

Studies with rabbit retina demonstrated that the region of minimum threshold for direct activation corresponds to the area of high-density sodium channels at the beginning of an axon in RGCs (Fried et al., 2009). This result is consistent with theoretical models of extracellular electrical stimulation, which predict that the intake of sodium on depolarized side of the membrane is responsible for triggering the action potential.

The probability of eliciting an action potential in RGCs increases with the stimulus amplitude following a sigmoidal function (Jepson et al., 2013; Fried et al., 2009). Stimulation thresholds in the literature usually correspond to a 50% probability of eliciting a response, although sometimes a 90% probability definition is used as well. A survey of available stimulation threshold data indicates that typically the charge density thresholds are in the range 0.1–1 mC/cm^2 with stimulation pulses not exceeding 1 ms (Sekirnjak et al., 2006).

1.39.4.1.1.2 Selective Stimulation of individual RGCs

The RGCs can generally respond to stimulation pulses at frequencies of at least 100 Hz (Sekirnjak et al., 2006; Cai et al., 2011), which makes it possible to produce naturalistic trains of action potentials by electrical stimulation (Jepson et al., 2014). Epiretinal implants that aim at restoring the natural visual code in each ganglion cell (Fried et al., 2006; Jepson et al., 2014) should be able to activate individual RGCs without affecting the surrounding cells. Different ganglion cell types were found to have somewhat different activation thresholds in the rabbit retina (Fried et al., 2009), likely due to differences in the sodium-channel bands and other anatomical or physiological properties. Selective activation of ganglion cells is very challenging: only about 7% of the RGCs could be activated selectively even in the peripheral primate retina (Grosberg et al., 2017), while in the central retina it is even harder due to thicker RGC layer and denser axonal bundles. Lack of selectivity in stimulation affects not only the ability to encode a natural retinal code, but also limits the spatial resolution.

Improving the selectivity of the RGCs activation has also been attempted by shaping of the electric field using dense arrays of microelectrodes. Encouraging results have been reported in the peripheral primate retina, where half of the somas of midget cells, which are thought to subtend high-acuity vision, could be activated without affecting surrounding parasol and small bistratified cell somas (Jepson et al., 2013). It is not known, however, whether these pulses affected the ~15 RGC types of the primate retina other than midget, parasol and SBCs in this study. It also remains unclear how well spatial activation strategies will work for the more central areas, where retinal ganglion cells stack up on top of one another, instead of forming a monolayer of cells, as in the periphery.

A major issue with epiretinal activation of RGCs is axonal stimulation (Grosberg et al., 2017; Weitz et al., 2015). Axons from distant cells are located in the nerve fiber layer, between the stimulating electrodes and the ganglion cells. Axonal stimulation thresholds are close to somatic ones (Behrend et al., 2011), and therefore epiretinal implants often activate not only the target RGCs, but also the axons of distant RGCs which pass close to the stimulating electrode, resulting in arcuate visual percepts (Nanduri et al., 2012). This effect, and the associated distortion of the retinotopic map, remains a major hurdle that epiretinal implants will need to overcome in order to provide meaningful visual percepts to blind patients. One approach for circumventing the problem of axonal stimulation is based on application of long (>20 ms) stimulation pulses to activate the inner nuclear layer rather than the ganglion cells (Weitz et al., 2015). Doing so significantly improves the localization of phosphenes in patients, however, it precludes encoding the retinal output by direct stimulation of the RGCs.

Another challenge with direct encoding of the proper spiking patterns in various types of RGCs is identification of the cell types in the degenerate retina. The RGCs are traditionally classified functionally on the basis of their light response properties (Chichilnisky and Kalmar, 2002). This method cannot work in a degenerate retina that has lost its photoreceptors. Instead, cell classification methods based on electrical signatures of the RGCs, called their electrophysiological images, have been proposed (Richard et al., 2015). However, applicability of this method to a degenerate retina, where spontaneous firing patterns become abnormal, remains to be tested.

1.39.4.1.2 Subretinal Stimulation

Subretinal implants aim at eliciting activity in the retinal ganglion cells by stimulating non-spiking (graded-response) neurons in the inner nuclear layer. The hope is to leverage some of the signal processing properties of the retinal network, and thereby create action potential patterns in the RGCs that resemble those arising under normal physiological conditions.

1.39.4.1.2.1 Stimulation thresholds

Stimulation threshold of a bipolar cell is defined by the voltage drop across it (Cho et al., 2016). It is assumed that retinal bipolar cells respond to stimulation by opening the Ca ion channels in their axon terminals (Haim, 2002), and that the response of the retinal ganglion cells (RGCs) is proportional to this output above a certain threshold, according to the linear-nonlinear model of retinal circuits (Tochitsky et al., 2014; Malmivuo and Plonsey, 1995a). In terms of current density, the stimulation threshold can be obtained from the retinal stimulation experiments with electrodes much larger than the retinal thickness, where uniform electric field approximation can be applied – for example with 0.5 mm wide electrodes in (Malmivuo and Plonsey, 1995b). For a 10 ms pulse, the threshold current density was $j = 1.3$ mA/cm^2, which corresponds to 13 μC/cm^2 charge density.

1.39.4.1.2.2 Dependence on Pulse Duration

Stimulation threshold varies with pulse duration according to the strength-duration curve, shown in **Fig. 3**C. Since the Na ion channels responsible for the RGC stimulation are much faster than Ca channels responsible for BPC stimulation, RGCs reach the rheobase much earlier than BPCs, whose stimulation threshold continues to decrease at least to 20 ms. Stimulation of BPCs with longer pulses enable higher selectivity of the network-mediated stimulation, i.e., eliciting response of BPCs without direct activation of RGCs. The fact that the number of action potentials in bursts that arise from the network-mediated electrical activation increases with stronger and longer stimuli (Mathieson et al., 2012; Tsai et al., 2009), makes it possible to encode the strength of the retinal response by controlling either the pulse amplitude or duration (**Fig. 9**).

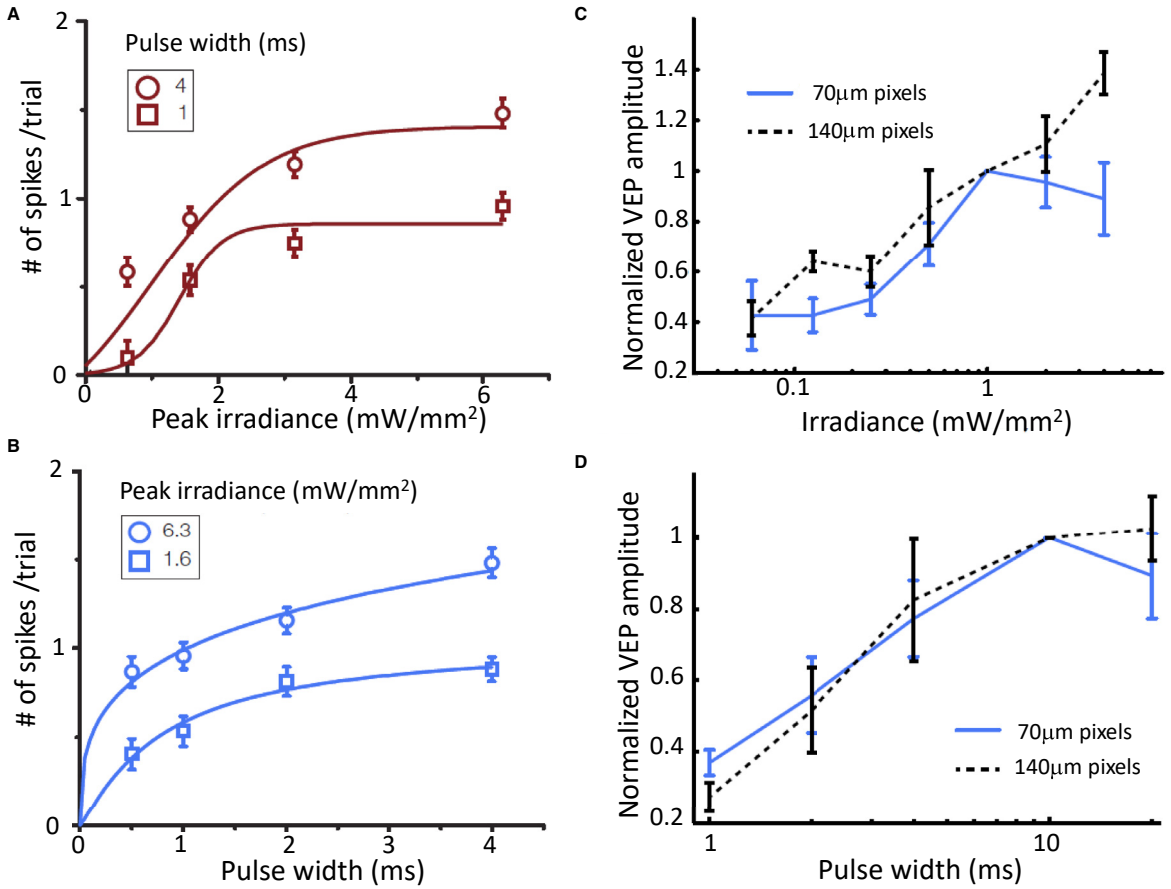

Figure 9 Modulation of Retinal and Cortical Responses by Pulse Width and Irradiance. The number of elicited spikes (within 65 ms post-stimulus) increases with irradiance **(A)** and with pulse width **(B)**. At the cortical level, **(C)** devices with 70 μm pixels (blue) elicit a VEP response at 0.25 mW/mm^2, which increases up to 1 mW/mm^2 and saturates beyond that level. The 140 μm pixels (black) have lower thresholds (0.12 mW/mm^2) and do not saturate at high irradiance. **(D)** VEP amplitude increases with pulse duration between 1 and 10 ms and saturates at longer pulses (with 2 and 4 mW/mm^2 irradiance for 140 μm and 70 μm pixel devices, respectively). Adapted from Mathieson et al. (2012) and Lorach et al. (2015b).

1.39.4.1.2.3 Frequency Response

As with natural vision, retinal response to network-mediated stimulation greatly diminishes with increasing activation frequency, dropping close to zero (<10%) at 20 Hz *ex-vivo* (Lorach et al., 2015b; Jensen and Rizzo, 2007); and at about 40 Hz in-vivo (Mandel et al., 2013; Ho et al., 2019) (**Fig. 10**). This decrease in retinal response has been initially described as "desensitization" (Freeman and Fried, 2011) of the retina, but was later identified as flicker fusion or "adaptation" to constant stimulation (Lorach et al., 2015b). With natural vision, such adaptation to high frequency stimulation is responsible for a continuous perception under fast stroboscopic illumination, such as in CRT or DLP displays. The extent of adaptation to repeated electrical stimulation varies greatly between cells: some stop responding to individual pulses at frequencies as low as 4 Hz, while other neurons do not adapt even at 40 Hz (Ho et al., 2018a).

1.39.4.1.2.4 Electric Receptive Fields

RGC receptive fields provide a description of the spatial extent of the visual field sampled by individual ganglion cells. Measuring them with prosthetic stimulation characterizes the combined point spread function of the implant and the retinal network (Lorach et al., 2015b; Sim et al., 2014). Using a multielectrode array to record from RGCs in the healthy and degenerate rat retina ex-vivo, their spatiotemporal properties were assessed from the spike-triggered average responses to a binary white noise stimulus at 20 Hz frame rate (Ho et al., 2018b). The average photovoltaic receptive field size with 70 μm pixels was 194 ± 3 μm, similar to that of natural visual responses - 221 ± 4 μm. Both visual and photovoltaic receptive fields in healthy retina had an opposing center-surround structure (Ho et al., 2018b). In the healthy retina, ON RGCs had photovoltaic OFF responses, and vice versa. This reversal is consistent with depolarization of photoreceptors by electrical pulses, as opposed to their hyperpolarization under increasing light, although alternative mechanisms cannot be excluded. In the degenerate rat retina, both ON and OFF photovoltaic responses were observed, ON – primarily in RGCs with low spontaneous firing rate and OFF – in cells with high spontaneous firing (Ho et al., 2018a). Interestingly, this seems to correspond to the natural ON and OFF RGCs since the ON cells in the degenerated rat retina exhibit low spontaneous firing, while OFF RGCs have high spontaneous firing rate (Sekirnjak et al., 2011). Degenerate retina maintained the antagonistic center-surround organization of receptive fields, most likely due to inhibitory response of the amacrine cells, as in normal retina.

1.39.4.1.2.5 Spatial Resolution

One of the most important characteristics of vision in general, and in prosthetic restoration of sight, in particular, is visual acuity. In normally-sighted rats, visual acuity evaluated through behavioral measurements is approximately 0.5–1 cycle per degree (Harnois et al., 1984), which corresponds to a much higher spatial resolution (15–30 μm on the retina) than the average size of receptive fields ($\sim 200\mu$m) (Lorach et al., 2015b). A possible explanation for this discrepancy is that RGCs also respond to movements of fine structures over their receptive fields (Thibos and Levick, 1983; Passaglia et al., 2002; Brown et al., 2000) thanks to nonlinear spatial integration of bipolar cell sub-units that connect to the same ganglion cell (Caldwell and Daw, 1978; Demb et al., 1999; Petrusca et al., 2007; Schwartz et al., 2012; Heine and Passaglia, 2011).

The hallmark of nonlinear spatial integration in a receptive field is a frequency doubling in the RGC response to alternating gratings presented over the extent of the receptive field (Heine and Passaglia, 2011; Victor and Shapley, 1979). Linear summation of the bipolar cells output in RGCs should lead to a constant ganglion cell output as a fine grating is alternated over the extent of the receptive field. However, a number of mechanisms can lead to nonlinear interactions between bipolar subunits (Borghuis et al., 2013), which, in turn, causes modulation of the RGC output when a fine texture moves over its receptive field. Extracting spatial location

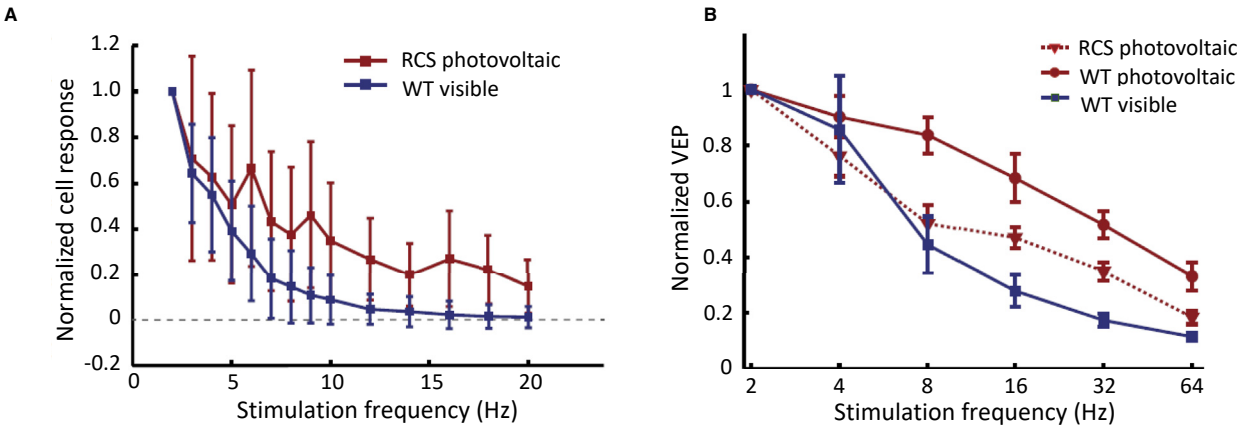

Figure 10 **Retinal and Cortical Adaptation to High Frequency Stimulation.** **(A)** Average steady-state response of RGCs to pulsed stimulation of varying frequency with visible (WT rats) and NIR (RCS rats) stimuli. **(B)** Normalized amplitude of the VEP response to visible (WT rats) and NIR (WT and RCS rats) stimulation of increasing frequency. Adapted from Lorach et al. (2015a).

information from non-linear subunit interactions in the receptive fields of RGCs would require a population-level decoding of the retinal signal by the brain.

Such nonlinear interactions have been measured in rats using alternating gratings projected over a subretinal photovoltaic array with a pixel pitch of 65 μm (Lorach et al., 2015b), and the results were compared to the response of the healthy retina to similar stimuli. The experiments were conducted with 20 Hz stimulus repetition rate and 1 Hz grating alternation. In healthy retina, very little, if any response to individual pulses of visible light were observed at 20 Hz, while RGCs responded strongly to the grating contrast reversal. Electrical stimulation resulted in a continuum of responses, ranging from a combination of very weak responses to individual pulses at 20 Hz and strong transient responses to the alternating grating, to more robust responses to every stimulation pulse. Neurons responded to electrical grating alternation with stripes down to 68 μm, and with visible light to 28 μm. RGC responses to the alternation of gratings smaller than their receptive fields showed evidence of frequency doubling, which indicates nonlinear subunit interactions (Lorach et al., 2015b). It also demonstrates that electrical stimulation can be spatially localized to subunits of the RGC receptive fields, and the width of the subunits matches the pixel pitch, indicating that smaller pixels might enable higher resolution.

1.39.4.1.2.6 Contrast Sensitivity

A similar MEA setup to that described above was used to compare the temporal contrast sensitivity of the natural and prosthetic vision. Degenerate rat retinas responded to photovoltaic stimulation with the contrast threshold of 12%, as opposed to 2.3% contrast steps with visible light stimulation of healthy retinas (Ho et al., 2018a). RGCs exhibited millisecond-scale variations in spike timing, even when the average firing rate did not change significantly. Response to the last pulse in the stimulation burst persisted longer than the steady-state response during the burst, which may be interpreted as an excitatory OFF response to prosthetic stimulation. Contrast enhancement of images prior to delivery to subretinal prosthesis is likely to be required to partially compensate for reduced contrast sensitivity of prosthetic vision.

1.39.4.2 Prosthetic Vision *In Vivo*

Vision is commonly quantified by resolution, contrast sensitivity and dynamic range, and these properties have been studied extensively with retinal implants (Lorach et al., 2015b; Ho et al., 2018a, 2018b, 2019; Behrend et al., 2011). Another important feature is the perception of motion, which is thought to be transmitted to the brain by the magnocellular-projecting parasol cells in the primate visual system (Merigan and Maunsell, 1993; Newsome et al., 1985). Accuracy of representation of motion signals with retinal prostheses has, so far, been explored only with epiretinal implants, for which promising results were reported with the elicitation of naturalistic motion stimuli in the peripheral primate retina (Jepson et al., 2014), even though this study did not address the possibility of unwanted axonal stimulation.

For *in-vivo* characterization, studies begin with implantation of the prosthesis in an adequate animal model. For example, a subretinal photovoltaic prosthesis can be implanted in a rat (Mandel et al., 2013) (**Fig. 11**). Surgery begins with a *trans*-scleral incision, followed by the creation of a retinal detachment using saline solution. The implant is then slid into the opening, which is subsequently sutured. Integration of the device into the subretinal space can be evaluated by Fluorescein angiography and optical coherence tomography (OCT) (**Fig. 10**B and C).

For evaluation of prosthetic vision, cortical signals, called Visually Evoked Potentials (VEP), can be measured via chronically implanted *trans*-cranial electrodes placed over the visual cortex (**Fig. 12**A). Corneal measurements of the waveforms produced by the implant can help evaluate charge injection by individual pixels and follow them over the lifetime of the animal (Lorach et al., 2015b). In addition, behavioral measurements have been used in assessment of the stimulation thresholds and contrast sensitivity (Ho et al., 2018a; Prevot et al., 2017).

1.39.4.2.1 Spatial Resolution

Visual acuity of prosthetic and natural vision was studied in rats using alternating grating patterns and recording the corresponding VEPs. With normal vision, this method matches well the visual acuity measured in behavioral tests (Silveira et al., 1987; Dean, 1981). For prosthetic vision in RCS rats implanted with photovoltaic arrays having 65 μm pixel pitch, the spatial resolution measured from visually evoked potentials was 64 ± 11 μm per stripe, as compared to 27 ± 9 μm per stripe in WT animals stimulated with visible light (Lorach et al., 2015b). These values correspond to 0.47 and 1.1 cycles per degree (cpd) respectively, in close agreement with the visual acuity of pigmented rats reported in the literature (Harnois et al., 1984). More recent measurements with 55 μm photovoltaic subretinal pixels demonstrated grating acuity of 48 ± 11 μm, which also matches the linear pixel pitch of the hexagonal array (Ho et al., 2019) (**Fig. 12**B). This geometrically corresponds to a visual acuity of 20/192 in a human eye – barely exceeding the threshold of legal blindness in the US (20/200). In these measurements natural acuity limit was 17 μm on the retina.

Behavioral tests of prosthetic vision in non-human primates using subretinal photovoltaic implants (PRIMA) with 100 μm pixels (Pixium Vision, Paris, France) demonstrated perceptual thresholds of 0.2 mW/mm^2 with 10 ms pulses (Prevot et al., 2017) - similar to the previous observations in rats (Ho et al., 2018a). These measurements, based on saccadic response to stimulation, demonstrated perception with a spot size down to a single pixel.

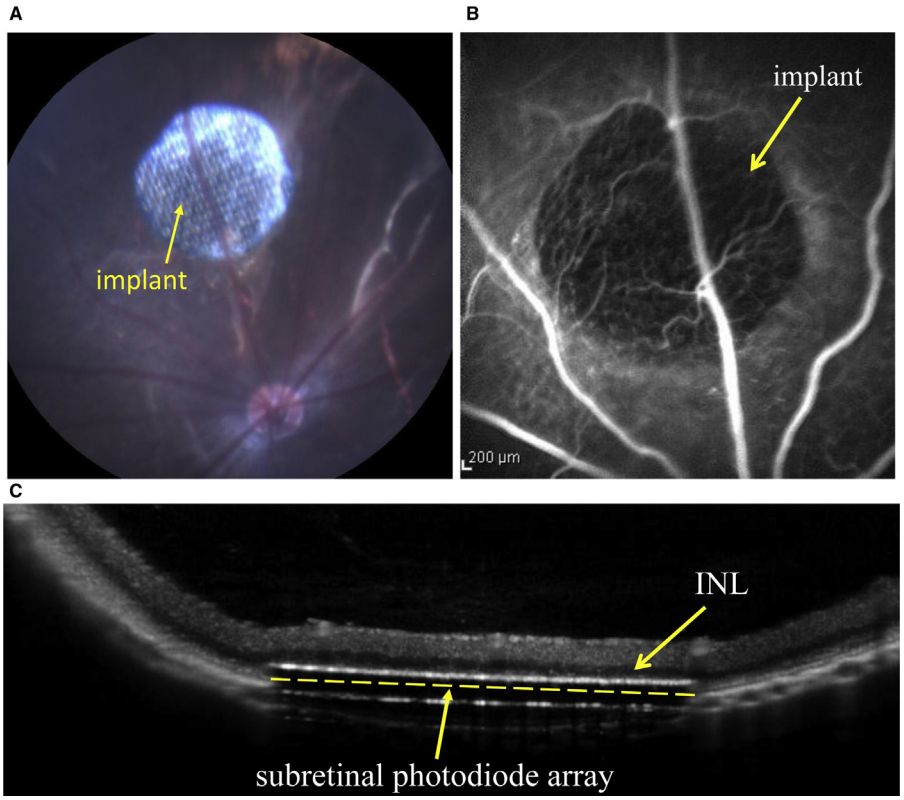

Figure 11 **Subretinal Implant In a Rat Eye.** (A) Fundus image of a subretinally implanted photovoltaic prosthesis with 70 μm pixels. **(B)** Fluorescein angiography of the RCS rat retina one week after implantation demonstrates normal retinal blood perfusion above the implant with no leakage. The implant is opaque to visible light and masks the choroidal fluorescence in the implanted area. Scale bar, 200 μm. **(C)** OCT shows good preservation of the inner retina, with the inner nuclear layer (INL, dark stipe) located ~20 μm above the upper surface of the implant (white line). The yellow dashed line illustrates the actual position of the back side of the implant, on top of the retinal pigment epithelium. Adapted from Lorach et al. (2015a).

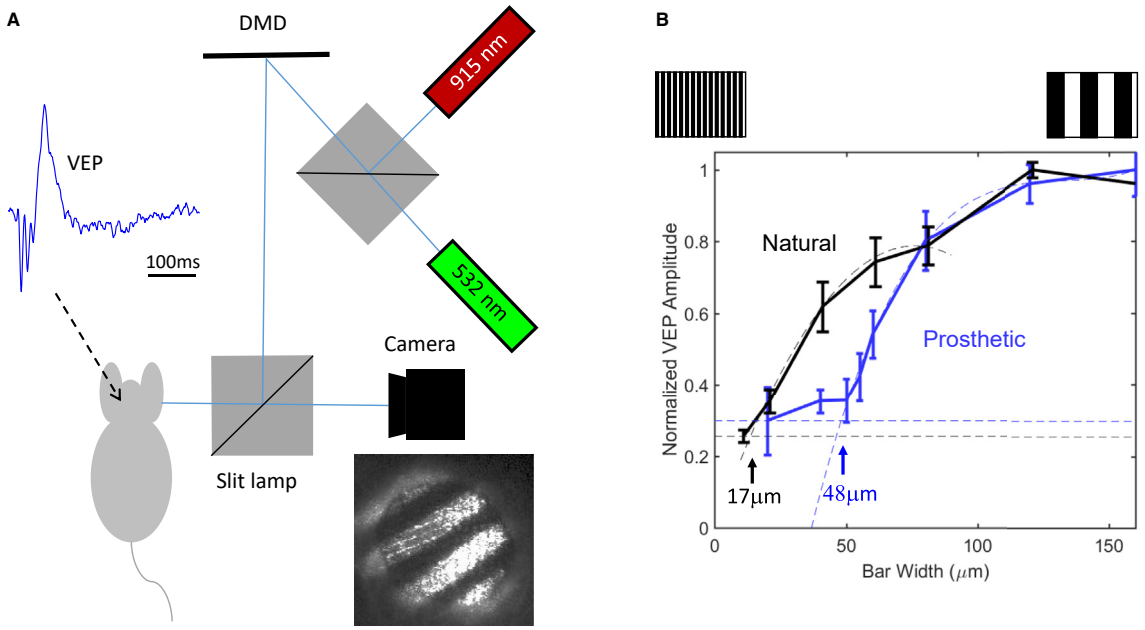

Figure 12 **Gratings Acuity Measurements In Vivo.** **(A)** Diagram of the experimental setup. Grating patterns are projected on the retina from DMD display using either visible or NIR light, and VEP response to grating alternation is measured. (B) Normalized VEP amplitude for visible gratings (black) and photovoltaic (prosthetic) stimulation (blue) as a function of the grating stripe width. The acuity limit, estimated as the crossing point of the parabolic fits with the noise level (dashed lines), corresponds to 17 ± 5 μm/stripe for visible light and 48 ± 11 μm/stripe for prosthetic stimulation. Adapted from Ho et al. (2019).

1.39.4.2.2 Contrast Sensitivity

To measure contrast sensitivity of prosthetic vision, blind rats (RCS) with photovoltaic subretinal prostheses were placed into cages surrounded by NIR LED displays. Two seconds long bursts at 20 Hz frequency were applied at various irradiance levels and pulse durations. Rats exhibited startling response to changes in brightness, with an average contrast threshold of 12%, as compared to 2.3% with visible light stimulation in healthy animals, matching the retinal response in MEA measurements *ex-vivo* described above (Ho et al., 2018a).

1.39.5 Clinical Results

The ultimate assessment of prosthetic vision is conducted by careful psychophysical evaluation of the visual percepts elicited in patients. A number of groups have reached this stage, thereby providing invaluable evidence that implants can elicit meaningful percepts in patients suffering from severe retinal degenerations. In this section, we review the current status and results of the clinical studies of various prosthetic devices.

1.39.5.1 Standards for Evaluating Prosthetic Vision

The FDA has issued non-binding recommendations on how to perform assessment of the visual function in their Investigational Device Exemption (IDE) Guidance for Retinal Prostheses (Cohen and Lepri, 2013). A set of low vision tests, called FLORA (Functional Low-vision Observer Rated Assessment), was introduced through the trial conducted by Second Sight Medical Implants (Sylmar, CA) of their Argus II retinal prosthesis (Ho et al., 2015). The tests suggested by the FDA include the following: (1) low vision letter acuity with limited response time; (2) grating acuity using a forced-choice paradigm and fixed presentation time; (3) mapping of stimulated visual phosphene fields, including two-point discrimination tests; (4) assessment of form vision and functional vision in real-world situations, including orientation and mobility.

Other clinical trials (Ayton et al., 2014; Stingl et al., 2015) have reported on static light perception, and often describe the perceived brightness, shape and color of those phosphenes. In addition to measurements of grating visual acuity, some patients could distinguish Landolt C-rings and read letters. Temporal characteristics of prosthetic vision and detection of motion are also frequently assessed.

1.39.5.2 The Argus II Epiretinal Implant

The only retinal prosthesis currently approved for commercial use by the FDA (as a humanitarian use device) is the Argus II epiretinal prosthetic system (Second Sight Medical Products, Sylmar, CA, United States). It consists of a head-mounted unit, which includes a camera and an RF antenna that transmits the processed data to the intraocular implant by serial telemetry (**Fig. 5**). The inductively-delivered signals are decoded and processed inside the implant, before being distributed over 60 stimulating electrodes via a *trans*-scleral cable. Electrodes are 200 μm in diameter, spaced by a 575 μm pitch (da Cruz et al., 2016), floating above the retina, on average, at 180 μm (Ahuja et al., 2013). The Argus II has been implanted in over 200 RP patients, with the best reported grating visual acuity of 20/1260 (Ho et al., 2015). A number of serious adverse events (SAEs) affecting approximately 30% of the patients were reported over the course of the clinical trial, the majority (82%) of which occurred within the first 6 months. Conjunctival erosion and dehiscence over the extraocular implant, were the most common occurrences (Ho et al., 2015). No device failures were reported within 3 years after implantation (Ho et al., 2015).

All subjects in the Argus II clinical trial were able to perceive light with the implant turned on, and almost all but one subjects performed better at square localization with the implant than without it. Only 57% of subjects performing better at detecting the direction of motion with the system ON than OFF. The clinical trial also reported improved orientation and mobility with the system, but other studies have reported the opposite, with a statistically significantly worsened performance at spatial orientation tasks with the implant on (Garcia et al., 2014). One reason for this discrepancy could be that the low-resolution visual percepts interfere with patient's natural orientation habits, including sounds and touch. Alternatively, Argus II could degrade spatial orientation since visual percepts it delivers are unrelated to the direction of gaze. Addition of the eye tracking and the corresponding image translation to the system indeed improves the object localization (Caspi et al., 2018).

A significant limitation of the Argus II implant is the stimulation of axons passing between the stimulating electrodes and the ganglion cells. As a result, percepts have arcuate rather than punctate shapes (Behrend et al., 2011; Nanduri et al., 2012), which severely distorts retinotopic mapping of the visual field. The most promising solution to this problem currently is based on application of much longer pulses (>25 ms instead of the typical 0.5–1 ms) to stimulate bipolar rather than ganglion cells, thereby invoking network-mediated retinal responses without axonal activation (Weitz et al., 2015).

None of the RP patients with ARGUS II regained vision to the extent that would allow ambulation without a white cane or a guide dog. In March 2019, Second Sight closed the ARGUS II project, and turned its focus to development and clinical evaluation of the cortical visual prosthesis, called Orion.

1.39.5.3 The Alpha IMS/AMS Subretinal Implant

The subretinal approach has been spearheaded in Germany by the Retina Implant AG (Reutlingen, Germany) with their Alpha-IMS system (Zrenner et al., 2011), which received CE mark in 2013. In this device, a subretinal camera (a CMOS chip consisting of photodiodes and amplifiers) converts images naturally projected onto the retina with ambient illumination into electrical currents that stimulate neurons in the inner nuclear layer (**Fig. 6**).

The implant consists of 1600 (40 × 40) pixels of 70 × 70 μm^2 in size, which include a photodiode, an amplifier and a 30 μm diameter SIROF electrode. Electrode array is 2.8 × 2.8 mm^2, corresponding to a visual field of 9.3°. Biphasic current pulses (cathodic phase first) with durations of 0.1–2.0 ms and frequency range of 0.5–500 Hz are applied to all electrodes synchronously. The sensitivity of the photodiode and the maximum stimulation current of the chip can be adjusted by the patient according to the ambient light intensity and individual retinal response (Stingl et al., 2017; Daschner et al., 2018). The return electrode is common to all the pixels in the implant and is located far from the stimulating electrodes. Power is delivered to the implant via a cable that runs underneath the retina through the sclera, and then under the skin, to a place behind the ear, where it is transferred inductively to the receiver with an RF transmitter (**Fig. 6**), like in cochlear implants.

Functional outcomes with foveal placement of the implant in RP patients ($n = 8$) were significantly better than with parafoveal placement ($n = 12$). No patients with nonfoveal placement could distinguish direction of motion, while 75% of the patients with foveal placement managed to accomplish this task (Stingl et al., 2013). Thirteen patients out of 15 participants in a trial had implant-mediated vision. Two patients were able to distinguish Landolt C of 20/546 acuity, which is about twice worse than the sampling density limit for the 70 μm pixel array (20/280). Twelve patients could achieve a basic grating acuity between 0.1 and 3.3 cpd. Detection, localization, and counting of objects was significantly better with the implant "ON" than with the implant "OFF" over the whole observation period. On average, 4.6 ± 0.8 gray levels could be distinguished.

Without stimulation, the eye movements of RP patients are large and scanning. With the implant ON, patients fixated well and exhibited classic fixational eye movement patterns, including ocular tremor, drift and microsaccades. After the stimuli disappeared, eye movements became large and scanning again (Hafed et al., 2016).

Majority of the Alpha IMS implants failed within a year post-implantation, while half of the Alpha AMS devices failed within 30 months (Daschner et al., 2018). In March 2019, Retina Implant AG was closed.

1.39.5.4 PRIMA: Photovoltaic Subretinal Implant

The wireless PRIMA implant (Pixium Vision, Paris) is designed for restoration of central vision in patients blinded by advanced AMD. Photovoltaic pixels directly convert projected light patterns into biphasic pulses of electric current (anodic phase first) (Lorach et al., 2015b). Array used in the first feasibility trial was 2 × 2 mm in size (corresponding to about 7 degrees of the visual angle in a human eye), 30 μm in thickness, with 378 pixels of 100 μm in width (Palanker, 2019). Images captured by the camera are processed and projected onto the retina from video glasses using NIR (880 nm) light to avoid photophobic and phototoxic effects of bright illumination (**Fig. 7**) (Goetz et al., 2013). For continuous perception under pulsed illumination, sufficiently high frequencies are applied (up to 30 Hz) to enable flicker fusion. Perceptual brightness is adjusted by modulating the pulse duration in the image from about 0.8 to 10 ms.

The feasibility study was conducted in five patients with geographic atrophy and a visual acuity 20/400–20/1000 in the worse-seeing "study" eye. Due to the surgical learning curve, in the first patient it was mistakenly implanted into the choroid, and in another it slipped under the retina by 2 mm toward the arcade. In the other 3 patients, sub-macular implant was placed centrally, as intended. All five patients perceived white-yellow patterns with adjustable brightness in retinotopically correct locations within the previous scotomata. All 4 patients with subretinal placement of the chip had Landolt C acuity, and the 3 patients with optimal placement of the implant demonstrated prosthetic acuity in the range of 20/460–20/550, which is 10%–30% below the theoretical sampling limit for the 100 μm pixel size (20/420) (Palanker, 2019). Residual natural acuity did not decrease after implantation in any of the patients, demonstrating the safety and stability of the sub-macular implantation of the wireless chip, with the follow-up now exceeding 12 months. The fact that prosthetic acuity closely matches the pixel pitch indicates that implants with smaller pixels might provide even higher acuity and hence more functional restoration of sight.

1.39.5.5 Other Clinical Systems

A suprachoroidal approach to restoration of sight has been pursued by Bionic Vision Australia (3 patients) (Ayton et al., 2014), and Osaka University (2 patients) (Fujikado et al., 2011). Phosphene perception remained over the 12-months Bionic Vision trial, but the equivalent visual acuity ranged from 20/4000 to 20/20,000 – well into the realm of ultra-low vision. Clinical trials of the IRIS II epiretinal implant with 150 electrodes have been conducted by Pixium Vision (Muqit et al., 2019) but discontinued since 2017. Optobionics conducted a clinical trial of their Artificial Silicon Retina (ASR) implant, which was a passive subretinal array of photodiodes. They reported improvements of central vision following implantation of the ASR in the periphery, possibly due to neurotrophic effects (Chow et al., 2004). The company closed in 2007, and trials did not continue. The EPIRET3 implant (Klauke et al., 2011) was implanted in 6 patients for a period of 4 weeks and successfully elicited visual percepts; however, no long-term study of the implant has been conducted to date.

1.39.6 Outlook

I conclude this review by suggesting some perspectives for future advancements in the field.

1.39.6.1 Improving Proximity to the Target Neurons in Subretinal Space

Distance between the implant and the target cells becomes a limiting factor when electrode size becomes comparable to, or smaller than the cell size, or when separation between the active and return electrode is similar to the distance to the target cells (Palanker et al., 2005; Loudin et al., 2007; Flores et al., 2019). Since INL is about 30–40 μm thick, planar subretinal implants with local return electrodes and pixel pitch smaller than 40 μm (20 μm radius) are unlikely to stimulate all the neurons in the INL within the safe charge injection limits (Flores et al., 2019). In addition, cross-talk between neighboring electrodes increases with the decreasing pixel size.

One way to improve proximity between the stimulating electrodes and the target neurons, is to use pillar electrodes on subretinal implants (**Fig. 4**B), which penetrate into the retina due to migration of the retinal cells into the voids between the pillars (Loudin et al., 2007; Butterwick et al., 2009). Recent measurements with 40 and 55 μm pixels in rats demonstrated that 10 μm tall pillar electrodes reduce stimulation threshold by half (Ho et al., 2019). However, this approach does not solve the fundamental problem limiting the electrode size - the shape of electric field, which expands radially from a small electrode and returns to another electrode under the target cells. Therefore, further decrease in the pixel size with pillar electrodes is unlikely.

A more fundamental solution to these limitations, which may enable scaling the pixels down to cellular dimensions is another 3-D geometry - the honeycomb configuration. In this approach, return electrodes are elevated on vertical insulating walls surrounding each pixel (**Fig. 4**C), which align the electric field vertically, matching the orientation of bipolar cells in the retina, and thereby reducing the stimulation threshold (Flores et al., 2019). These walls also decouple the field penetration depth from the pixel width, enabling a decrease of the pixel size down to cellular dimensions while maintaining the same stimulation threshold. Like with pillar electrodes, this approach leverages migration of retinal cells into voids larger than about 10 μm in subretinal space.

One caveat with 3-dimensional implants is that they will be more difficult to explant, since the retina integrates into them, and careful biocompatibility and long-term stability studies will be required before they can be implanted into patients.

1.39.6.2 Epiretinal Implant With Bi-directional Telemetry

A new group recently formed to develop "artificial retina" – a device capable of closely mimicking normal retinal function and interfacing with the retinal ganglion cells for proper restoration of sight to the blind. This system aims at reproducing the precise retinal code at cellular resolution with cell-type specificity, enabling high-fidelity artificial vision (Shah et al., 2019). This approach is based on two-step process: an initial calibration, followed by real-time activation of the implant. For calibration, the implanted electrode array will record and identify the many distinct ganglion cell types based on characteristics of their spontaneous firing. This should result in a map of which electrodes can efficiently stimulate particular ganglion cells under the array. To reproduce a desired artificial visual stimulus, the implant will use the dictionary of achievable electrical stimulation patterns from the memory and activate the appropriate ganglion cells at the appropriate times, effectively transforming any incoming visual scene into properly timed activity of the various types of RGCs.

For this system to work, it has to overcome many challenges: (a) selective activation of RGCs in a multilayered ganglion cell layer while avoiding axonal stimulation; (b) cell type identification based on spontaneous firing, which is altered by retinal degeneration; (c) micrometer-scale stability of the implant relative to the retina in order to maintain the stable calibration map; (d) knowledge of the "retinal code" for natural scenes.

1.39.6.3 Image Processing

Significant opportunities for improving prosthetic vision might come from more advanced image processing. Virtual and augmented reality devices are becoming more common, and computers are getting better at understanding the features of the visual world. Obvious steps would include optical or electronic zoom, contrast enhancement and autofocus of the camera. Simplification of the visual scenes prior to its display to the eye may help better match its resolution and contrast sensitivity limits and make visual percepts easier to understand. Several groups have already demonstrated promising results by segregating the visual content of a scene by distance, and displaying only the closer objects (Jung et al., 2015), or by encoding depth instead of luminance information to facilitate navigation (Hicks et al., 2014). Other improvements may include symbolic representation of the objects, such as banknotes, as well as integration of the assistive technologies unrelated to prosthetic vision, such as the face recognition, text-to-voice conversion, etc.

1.39.6.4 Brain Plasticity and the Retinal Code: How Much Fidelity Do We Need?

The need for a complete and accurate restoration of the visual code in retinal stimulation is being actively debated. Based on preclinical data and the recent results with PRIMA implant in AMD patients, proponents of the subretinal implants argue that a device providing retinotopically correct stimulation of bipolar cells with high resolution should be able to deliver meaningful visual

percepts to patients. They hope that the brain will be able to interpret or learn a new "prosthetic language", as long as the stimulation utilizes the retinal neural network, retinotopic map is preserved, contrast modulation is monotonic, and the signals are reproducible. Others, in favor of an epiretinal approach (Jepson et al., 2014), argue that functional restoration of sight will be attained only if the proper visual code is delivered directly to, at least, the most prevalent types of ganglion cells. This debate is likely to continue until each type of the implants is extensively tested in patients, its limitations established, and behavioral performance is carefully assessed.

1.39.7 Summary and Conclusions

The first two companies which attempted restoration of sight in patients blinded by inherited retinal degeneration (RP) using epiretinal (ARGUS II by Second Sight) and subretinal (Alpha IMS/AMS by Retina Implant AG) implants have proven the principle, but failed to reach the acceptable performance and discontinued their products in 2019, after about 20 years of development. The next generation of implants is designed to address their shortcomings. For example, the photovoltaic subretinal implant PRIMA is completely wireless, and hence can be used in AMD patients, where retinal network is much better preserved than in the end-stage RP. In addition, local return electrodes provide much better confinement of electric field around each pixel, thereby improving selectivity, resolution and contrast of the stimulation patterns. As a result, patients with PRIMA demonstrate shaped prosthetic vision with acuity levels close to the current pixel size. The next challenge is to scale the pixels down to, ideally, below 25 μm, in order to restore central vision with acuity better than 20/100, which would provide real benefit for patients blinded by AMD. An alternative approach under development is the epiretinal implant (Artificial Retina) for selective activation of the many classes of RGCs with the appropriate retinal code in order to restore sight in the end-stage RP patients despite strong rewiring of the retinal network. This project faces many technical challenges, but if successful, it has the potential to properly restore many features of natural vision. Commercialization of such complex technology is another challenge, and therefore these developments are usually undertaken by consortiums of the academic groups and commercial entities.

References

Ahuja, A.K., Dorn, J.D., Caspi, A., McMahon, M.J., Dagnelie, G., Dacruz, L., Stanga, P., Humayun, M.S., Greenberg, R.J., 2011. Blind subjects implanted with the Argus II retinal prosthesis are able to improve performance in a spatial-motor task. Br. J. Ophthalmol. 95 (4), 539–543.

Ahuja, A.K., Yeoh, J., Dorn, J.D., Caspi, A., Wuyyuru, V., McMahon, M.J., Humayun, M.S., Greenberg, R.J., Dacruz, L., 2013. Factors affecting perceptual threshold in Argus II retinal prosthesis subjects. Transl. Vis. Sci. Technol. 2 (4), 1.

Anderson, D.J., Najafi, K., Tanghe, S.J., Evans, D.A., Levy, K.L., Hetke, J.F., Xue, X.L., Zappia, J.J., Wise, K.D., 1989. Batch-fabricated thin-film electrodes for stimulation of the central auditory-system. IEEE Trans. Biomed. Eng. 36 (7), 693–704.

Ayton, L.N., Blamey, P.J., Guymer, R.H., Luu, C.D., Nayagam, D.A., Sinclair, N.C., Shivdasani, M.N., Yeoh, J., McCombe, M.F., Briggs, R.J., et al., 2014. First-in-human trial of a novel suprachoroidal retinal prosthesis. PLoS One 9 (12), e115239.

Barlow, H.B., Hill, R.M., Levick, W.R., 1964. Retinal ganglion cells responding selectively to direction and speed of image motion in the rabbit. J. physiol. 173, 377–407.

Behrend, M.R., Ahuja, A.K., Humayun, M.S., Chow, R.H., Weiland, J.D., 2011. Resolution of the epiretinal prosthesis is not limited by electrode size. IEEE Trans. Neural. Syst. Rehabil. Eng. 19 (4), 436–442.

Bendali, A., Agnes, C., Meffert, S., Forster, V., Bongrain, A., Arnault, J.C., Sahel, J.A., Offenhausser, A., Bergonzo, P., Picaud, S., 2014. Distinctive glial and neuronal interfacing on nanocrystalline diamond. PLoS One 9 (3).

Boinagrov, D., Loudin, J., Palanker, D., 2010. Strength-duration relationship for extracellular neural stimulation: numerical and analytical models. J. Neurophysiol. 104 (4), 2236–2248.

Boinagrov, D., Pangratz-Fuehrer, S., Suh, B., Mathieson, K., Naik, N., Palanker, D., 2012. Upper threshold of extracellular neural stimulation. J. Neurophysiol. 108 (12), 3233–3238.

Boinagrov, D., Pangratz-Fuehrer, S., Goetz, G., Palanker, D., 2014. Selectivity of direct and network-mediated stimulation of the retinal ganglion cells with epi-, sub- and intraretinal electrodes. J. Neural. Eng. 11 (2), 026008.

Boinagrov, D., Lei, X., Goetz, G., Kamins, T.I., Mathieson, K., Galambos, L., Harris, J.S., Palanker, D., 2016. Photovoltaic pixels for neural stimulation: circuit models and performance. IEEE Trans. Biomed. Circuits Syst. 10 (1), 85–97.

Bolz, A., Amon, M., Ozbek, C., Heublein, B., Schaldach, M., 1996. Coating of cardiovascular stents with a semiconductor to improve their hemocompatibility. Tex. Heart Inst. J. 23 (2), 162–166.

Borghuis, B.G., Marvin, J.S., Looger, L.L., Demb, J.B., 2013. Two-photon imaging of nonlinear glutamate release dynamics at bipolar cell synapses in the mouse retina. J. Neurosci. 33 (27), 10972–10985.

Bostock, H., 1983. The strength-duration relationship for excitation of myelinated nerve: computed dependence on membrane parameters. J. physiol. 341, 59–74.

Briggman, K.L., Helmstaedter, M., Denk, W., 2011. Wiring specificity in the direction-selectivity circuit of the retina. Nature 471 (7337), 183–188.

Britten, K.H., Shadlen, M.N., Newsome, W.T., Movshon, J.A., 1992. The analysis of visual motion: a comparison of neuronal and psychophysical performance. J. Neurosci. 12 (12), 4745–4765.

Brown, S.P., He, S., Masland, R.H., 2000. Receptive field microstructure and dendritic geometry of retinal ganglion cells. Neuron 27 (2), 371–383.

Butterwick, A., Vankov, A., Huie, P., Freyvert, Y., Palanker, D., 2007. Tissue damage by pulsed electrical stimulation. IEEE Trans. Biomed. Eng. 54 (12), 2261–2267.

Butterwick, A., Huie, P., Jones, B.W., Marc, R.E., Marmor, M., Palanker, D., 2009. Effect of shape and coating of a subretinal prosthesis on its integration with the retina. Exp. Eye Res. 88 (1), 22–29.

Cai, C., Ren, Q., Desai, N.J., Rizzo 3rd, J.F., Fried, S.I., 2011. Response variability to high rates of electric stimulation in retinal ganglion cells. J. Neurophysiol. 106 (1), 153–162.

Caldwell, J.H., Daw, N.W., 1978. New properties of rabbit retinal ganglion cells. J. physiol. 276, 257–276.

Caspi, A., Roy, A., Wuyyuru, V., Rosendall, P.E., Harper, J.W., Katyal, K.D., Barry, M.P., Dagnelie, G., Greenberg, R.J., 2018. Eye movement control in the Argus II retinal-prosthesis enables reduced head movement and better localization precision. Invest. Ophthalmol. Vis. Sci. 59 (2), 792–802.

Chang, B., Hawes, N.L., Hurd, R.E., Davisson, M.T., Nusinowitz, S., Heckenlively, J.R., 2002. Retinal degeneration mutants in the mouse. Vision Res. 42 (4), 517–525.

Chen, Y.C., Tsai, C.Y., Lee, C.Y., Lin, I.N., 2014. In vitro and in vivo evaluation of ultrananocrystalline diamond as an encapsulation layer for implantable microchips. Acta Biomater. 10 (5), 2187–2199.
Chichilnisky, E.J., Kalmar, R.S., 2002. Functional asymmetries in ON and OFF ganglion cells of primate retina. J. Neurosci. 22 (7), 2737–2747.
Cho, A., Ratliff, C., Sampath, A., Weiland, J., 2016. Changes in ganglion cell physiology during retinal degeneration influence excitability by prosthetic electrodes. J. Neural. Eng. 13 (2), 025001.
Chow, A.Y., Chow, V.Y., Packo, K.H., Pollack, J.S., Peyman, G.A., Schuchard, R., 2004. The artificial silicon retina microchip for the treatment of vision loss from retinitis pigmentosa. Arch. Ophthalmol. 122 (4), 460–469.
Cogan, S.F., 2008. Neural stimulation and recording electrodes. Annu. Rev. Biomed. Eng. 10, 275–309.
Cohen, E., Lepri, B., 2013. Investigational device exemption guidance for retinal prostheses. In: Center for Devices and Radiological Health FaDA.
da Cruz, L., Dorn, J.D., Humayun, M.S., Dagnelie, G., Handa, J., Barale, P.O., Sahel, J.A., Stanga, P.E., Hafezi, F., Safran, A.B., et al., 2016. Five-year safety and performance results from the Argus II retinal prosthesis system clinical trial. Ophthalmol. 123 (10), 2248–2254.
Daschner, R., Greppmaier, U., Kokelmann, M., Rudorf, S., Rudorf, R., Schleehauf, S., Wrobel, W.G., 2017. Laboratory and clinical reliability of conformally coated subretinal implants. Biomed. Microdevices 19 (1).
Daschner, R., Rothermel, A., Rudorf, R., Rudorf, S., Stett, A., 2018. Functionality and performance of the subretinal implant chip Alpha AMS. Sensor. Mater. 30 (2), 179–192.
Dean, P., 1981. Visual pathways and acuity hooded rats. Behav. Brain Res. 3 (2), 239–271.
Delori, F.C., Webb, R.H., Sliney, D.H., 2007. Maximum permissible exposures for ocular safety (ANSI 2000), with emphasis on ophthalmic devices. J. Opt. Soc. Am. A 24 (5), 1250–1265.
Demb, J.B., Haarsma, L., Freed, M.A., Sterling, P., 1999. Functional circuitry of the retinal ganglion cell's nonlinear receptive field. J. Neurosci. 19 (22), 9756–9767.
Field, G.D., Sher, A., Gauthier, J.L., Greschner, M., Shlens, J., Litke, A.M., Chichilnisky, E.J., 2007. Spatial properties and functional organization of small bistratified ganglion cells in primate retina. J. Neurosci. 27 (48), 13261–13272.
Flores, T., Goetz, G., Lei, X., Palanker, D., 2016. Optimization of return electrodes in neurostimulating arrays. J. Neural. Eng. 13 (3), 036010.
Flores, T., Huang, T., Bhuckory, M., Ho, E., Chen, Z., Dalal, R., Galambos, L., Kamins, T., Mathieson, K., Palanker, D., 2019. Honeycomb-shaped electro-neural interface enables cellular-scale pixels in subretinal prosthesis. Sci. Rep. 9 (1), 10657.
Freeman, D.K., Fried, S.I., 2011. Multiple components of ganglion cell desensitization in response to prosthetic stimulation. J. Neural. Eng. 8 (1), 016008.
Fried, S.I., Hsueh, H.A., Werblin, F.S., 2006. A method for generating precise temporal patterns of retinal spiking using prosthetic stimulation. J. Neurophysiol. 95 (2), 970–978.
Fried, S.I., Lasker, A.C.W., Desai, N.J., Eddington, D.K., Rizzo, J.F., 2009. Axonal sodium-channel bands shape the response to electric stimulation in retinal ganglion cells. J. Neurophysiol. 101 (4), 1972–1987.
Friedman, D.S., Tomany, S.C., McCarty, C., De Jong, P., 2004. Prevalence of age-related macular degeneration in the United States. Arch. Ophthalmol. 122 (4), 564–572.
Fujikado, T., Kamei, M., Sakaguchi, H., Kanda, H., Morimoto, T., Ikuno, Y., Nishida, K., Kishima, H., Maruo, T., Konoma, K., et al., 2011. Testing of semichronically implanted retinal prosthesis by suprachoroidal-transretinal stimulation in patients with retinitis pigmentosa. Invest. Ophthalmol. Vis. Sci. 52 (7), 4726–4733.
Garcia, S., Petrini, K., Da Cruz, L., Rubin, G.S., Nardini, M., 2014. Assessing improvements in perception afforded by retinal prostheses in multisensory tasks. Invest. Ophthalmol. Vis. Sci. 55 (13).
Ghezzi, D., Antognazza, M.R., Maccarone, R., Bellani, S., Lanzarini, E., Martino, N., Mete, M., Pertile, G., Bisti, S., Lanzani, G., et al., 2013. A polymer optoelectronic interface restores light sensitivity in blind rat retinas. Nat. Photon. 7 (5), 400–406.
Goetz, G.A., Mandel, Y., Manivanh, R., Palanker, D.V., Cizmar, T., 2013. Holographic display system for restoration of sight to the blind. J. Neural. Eng. 10 (5).
Greschner, M., Field, G.D., Li, P.H., Schiff, M.L., Gauthier, J.L., Ahn, D., Sher, A., Litke, A.M., Chichilnisky, E.J., 2014. A polyaxonal amacrine cell population in the primate retina. J. Neurosci. 34 (10), 3597–3606.
Grosberg, L.E., Ganesan, K., Goetz, G.A., Madugula, S.S., Bhaskhar, N., Fan, V., Li, P., Hottowy, P., Dabrowski, W., Sher, A., et al., 2017. Activation of ganglion cells and axon bundles using epiretinal electrical stimulation. J. Neurophysiol. 118 (3), 1457–1471.
Grover, S., Fishman, G.A., Anderson, R.J., Tozatti, M.S., Heckenlively, J.R., Weleber, R.G., Edwards, A.O., Brown Jr., J., 1999. Visual acuity impairment in patients with retinitis pigmentosa at age 45 years or older. Ophthalmology 106 (9), 1780–1785.
Ha, S., Khraiche, M.L., Akinin, A., Jing, Y., Damle, S., Kuang, Y., Bauchner, S., Lo, Y.H., Freeman, W.R., Silva, G.A., et al., 2016. Towards high-resolution retinal prostheses with direct optical addressing and inductive telemetry. J. Neural. Eng. 13 (5), 056008.
Hadjinicolaou, A.E., Leung, R.T., Garrett, D.J., Ganesan, K., Fox, K., Nayagam, D.A.X., Shivdasani, M.N., Meffin, H., Ibbotson, M.R., Prawer, S., et al., 2012. Electrical stimulation of retinal ganglion cells with diamond and the development of an all diamond retinal prosthesis. Biomaterials 33 (24), 5812–5820.
Hafed, Z.M., Stingl, K., Bartz-Schmidt, K.U., Gekeler, F., Zrenner, E., 2016. Oculomotor behavior of blind patients seeing with a subretinal visual implant. Vision Res. 118, 119–131.
Haim, M., 2002. Epidemiology of retinitis pigmentosa in Denmark. Acta Ophthalmol. Scand. Suppl. (233), 1–34.
Harnois, C., Bodis-Wollner, I., Onofrj, M., 1984. The effect of contrast and spatial frequency on the visual evoked potential of the hooded rat. Exp. Brain Res. 57 (1), 1–8.
Heine, W.F., Passaglia, C.L., 2011. Spatial receptive field properties of rat retinal ganglion cells. Vis. Neurosci. 28 (5), 403–417.
Hicks, S.L., Wilson, I., van Rheede, J.J., MacLaren, R.E., Downes, S.M., Kennard, C., 2014. Improved mobility with depth-based residual vision glasses. Invest. Ophth. Vis. Sci. 55 (13).
Ho, A.C., Humayun, M.S., Dorn, J.D., da Cruz, L., Dagnelie, G., Handa, J., Barale, P.O., Sahel, J.A., Stanga, P.E., Hafezi, F., et al., 2015. Long-term results from an epiretinal prosthesis to restore sight to the blind. Ophthalmology 122 (8), 1547–1554.
Ho, E., Lorach, H., Goetz, G., Laszlo, F., Lei, X., Kamins, T., Mariani, J.C., Sher, A., Palanker, D., 2018a. Temporal structure in spiking patterns of ganglion cells defines perceptual thresholds in rodents with subretinal prosthesis. Sci. Rep. 8 (1), 3145.
Ho, E., Smith, R., Goetz, G., Lei, X., Galambos, L., Kamins, T.I., Harris, J., Mathieson, K., Palanker, D., Sher, A., 2018b. Spatiotemporal characteristics of retinal response to network-mediated photovoltaic stimulation. J. Neurophysiol. 119 (2), 389–400.
Ho, E., Lei, X., Flores, T.A., Lorach, H., Huang, T.W., Galambos, L., Kamins, T., Harris, J.S., Mathieson, K., Palanker, D., 2019. Characteristics of prosthetic vision in rats with subretinal flat and pillar electrode arrays. J. Neural. Eng. 16 (6).
Hornig, R., Dapper, M., Le Joliff, E., Hill, R., Ishaque, K., Posch, C., Benosman, R., LeMer, Y., Sahel, J.-A., Picaud, S., 2017. Pixium vision: first clinical results and innovative developments. In: Gabel, V.P. (Ed.), Artificial Vision: A Clinical Guide, edn. Springer International Publishing, Cham, pp. 99–113.
Hsu, J.M., Rieth, L., Normann, R.A., Tathireddy, P., Solzbacher, F., 2009. Encapsulation of an integrated neural interface device with Parylene C. IEEE Trans. Biomed. Eng. 56 (1), 23–29.
Huberman, A.D., Niell, C.M., 2011. What can mice tell us about how vision works? Trends Neurosci. 34 (9), 464–473.
Humayun, M., Propst, R., Dejuan, E., Mccormick, K., Hickingbotham, D., 1994. Bipolar surface electrical-stimulation of the vertebrate retina. Arch. Ophthalmol. 112 (1), 110–116.
Humayun, M.S., Prince, M., de Juan, E., Barron, Y., Moskowitz, M., Klock, I.B., Milam, A.H., 1999. Morphometric analysis of the extramacular retina from postmortem eyes with retinitis pigmentosa. Invest. Ophth. Vis. Sci. 40 (1), 143–148.
Humayun, M.S., Dorn, J.D., da Cruz, L., Dagnelie, G., Sahel, J.A., Stanga, P.E., Cideciyan, A.V., Duncan, J.L., Eliott, D., Filley, E., et al., 2012. Interim results from the international trial of Second Sight's visual prosthesis. Ophthalmology 119 (4), 779–788.
Iridium Medical Technologies, Hsinchu City, Taiwan(R.O.C), [http://www.irmedtech.com/Advantage/index_en.html].
Jensen, R.J., Rizzo 3rd, J.F., 2006. Thresholds for activation of rabbit retinal ganglion cells with a subretinal electrode. Exp. Eye Res. 83 (2), 367–373.
Jensen, R.J., Rizzo 3rd, J.F., 2007. Responses of ganglion cells to repetitive electrical stimulation of the retina. J. Neural. Eng. 4 (1), S1–S6.

Jensen, R.J., Rizzo 3rd, J.F., Ziv, O.R., Grumet, A., Wyatt, J., 2003. Thresholds for activation of rabbit retinal ganglion cells with an ultrafine, extracellular microelectrode. Invest. Ophthalmol. Vis. Sci. 44 (8), 3533–3543.
Jensen, R.J., Ziv, O.R., Rizzo 3rd, J.F., 2005. Thresholds for activation of rabbit retinal ganglion cells with relatively large, extracellular microelectrodes. Invest. Ophthalmol. Vis. Sci. 46 (4), 1486–1496.
Jepson, L.H., Hottowy, P., Mathieson, K., Gunning, D.E., Dabrowski, W., Litke, A.M., Chichilnisky, E.J., 2013. Focal electrical stimulation of major ganglion cell types in the primate retina for the design of visual prostheses. J. Neurosci. 33 (17), 7194–7205.
Jepson, L.H., Hottowy, P., Weiner, G.A., Dabrowski, W., Litke, A.M., Chichilnisky, E.J., 2014. High-fidelity reproduction of spatiotemporal visual signals for retinal prosthesis. Neuron 83 (1), 87–92.
Jones, B.W., Marc, R.E., 2005. Retinal remodeling during retinal degeneration. Exp. Eye Res. 81 (2), 123–137.
Jung, J.H., Aloni, D., Yitzhaky, Y., Peli, E., 2015. Active confocal imaging for visual prostheses. Vision Res. 111 (Pt B), 182–196.
Kane, S.R., Cogan, S.F., Ehrlich, J., Plante, T.D., McCreery, D.B., Troyk, P.R., 2013. Electrical performance of penetrating microelectrodes chronically implanted in cat cortex. IEEE Trans. Biomed. Eng. 60 (8), 2153–2160.
Kim, S.Y., Sadda, S., Pearlman, J., Humayun, M.S., de Juan Jr., E., Melia, B.M., Green, W.R., 2002. Morphometric analysis of the macula in eyes with disciform age-related macular degeneration. Retina 22 (4), 471–477.
Klauke, S., Goertz, M., Rein, S., Hoehl, D., Thomas, U., Eckhorn, R., Bremmer, F., Wachtler, T., 2011. Stimulation with a wireless intraocular epiretinal implant elicits visual percepts in blind humans. Invest. Ophthalmol. Vis. Sci. 52 (1), 449–455.
Knutson, J.S., Naples, G.G., Peckham, P.H., Keith, M.W., 2002. Electrode fracture rates and occurrences of infection and granuloma associated with percutaneous intramuscular electrodes in upper-limb functional electrical stimulation applications. J. Rehabil. Res. Dev. 39 (6), 671–683.
Lee, D.Y., Lorach, H., Huie, P., Palanker, D., 2016. Implantation of modular photovoltaic subretinal prosthesis. Ophthalmic. Surg. Lasers Imaging Retina 47 (2), 171–174.
Lei, X., Kane, S., Cogan, S., Lorach, H., Galambos, L., Huie, P., Mathieson, K., Kamins, T., Harris, J., Palanker, D., 2016. SiC protective coating for photovoltaic retinal prosthesis. J. Neural. Eng. 13 (4).
Liu, W.T., Vichienchom, K., Clements, M., DeMarco, S.C., Hughes, C., McGucken, E., Humayun, M.S., de Juan, E., Weiland, J.D., Greenberg, R., 2000. A neuro-stimulus chip with telemetry unit for retinal prosthetic device. IEEE J. Solid State Circ. 35 (10), 1487–1497.
Loeb, G., Bak, M., Salcman, M., Schmidt, E., 1977. Parylene as a chronically stable, reproducible microelectrode insulator. IEEE Trans. Biomed. Eng. 24 (2), 121–128.
Lorach, H., Kung, J., Beier, C., Mandel, Y., Dalal, R., Huie, P., Wang, J., Lee, S., Sher, A., Jones, B.W., et al., 2015a. Development of animal models of local retinal degeneration. Invest. Ophthalmol. Vis. Sci. 56 (8), 4644–4652.
Lorach, H., Goetz, G., Smith, R., Lei, X., Mandel, Y., Kamins, T., Mathieson, K., Huie, P., Harris, J., Sher, A., et al., 2015b. Photovoltaic restoration of sight with high visual acuity. Nat. Med. 21 (5), 476–482.
Lorach, H., Wang, J., Lee, D.Y., Dalal, R., Huie, P., Palanker, D., 2016. Retinal safety of near infrared radiation in photovoltaic restoration of sight. Biomed. Optic Express 7 (1), 13–21.
Loudin, J.D., Simanovskii, D.M., Vijayraghavan, K., Sramek, C.K., Butterwick, A.F., Huie, P., McLean, G.Y., Palanker, D.V., 2007. Optoelectronic retinal prosthesis: system design and performance. J. Neural. Eng. 4 (1), S72–S84.
Malmivuo, J., Plonsey, R., 1995a. Subthreshold membrane phenomena. In: Bioelectromagnetism. Oxford University Press, New York, pp. 44–65.
Malmivuo, J., Plonsey, R., 1995b. Hodgkin-huxley membrane model. In: Bioelectromagnetism. Oxford University Press, New York, pp. 74–93.
Malmivuo, J., Plonsey, R., 1995c. Functional electric stimulation. In: Bioelectromagnetism. Oxford University Press, New York, pp. 363–375.
Mandel, Y., Goetz, G., Lavinsky, D., Huie, P., Mathieson, K., Wang, L., Kamins, T., Galambos, L., Manivanh, R., Harris, J., et al., 2013. Cortical responses elicited by photovoltaic subretinal prostheses exhibit similarities to visually evoked potentials. Nat. Commun. 4, 1980.
Manookin, M.B., Patterson, S.S., Linehan, C.M., 2018. Neural mechanisms mediating motion sensitivity in parasol ganglion cells of the primate retina. Neuron 97 (6), 1327–1340.e1324.
Marc, R.E., Jones, B.W., 2003. Retinal remodeling in inherited photoreceptor degenerations. Mol. Neurobiol. 28 (2), 139–147.
Marc, R.E., Jones, B.W., Watt, C.B., Strettoi, E., 2003. Neural remodeling in retinal degeneration. Prog. Retin. Eye Res. 22 (5), 607–655.
Margolis, D.J., Newkirk, G., Euler, T., Detwiler, P.B., 2008. Functional stability of retinal ganglion cells after degeneration-induced changes in synaptic input. J. Neurosci. 28 (25), 6526–6536.
Masland, R.H., 2001. The fundamental plan of the retina. Nat. Neurosci. 4 (9), 877–886.
Mathieson, K., Loudin, J., Goetz, G., Huie, P., Wang, L., Kamins, T.I., Galambos, L., Smith, R., Harris, J.S., Sher, A., et al., 2012. Photovoltaic retinal prosthesis with high pixel density. Nat. Photon. 6 (6), 391–397.
Mazzoni, F., Novelli, E., Strettoi, E., 2008. Retinal ganglion cells survive and maintain normal dendritic morphology in a mouse model of inherited photoreceptor degeneration. J. Neurosci. 28 (52), 14282–14292.
Mccreery, D.B., Agnew, W.F., Yuen, T.G.H., Bullara, L., 1990. Charge-density and charge per phase as cofactors in neural injury induced by electrical-stimulation. IEEE Trans. Biomed. Eng. 37 (10), 996–1001.
McIntyre, C.C., Grill, W.M., 1998. Sensitivity analysis of a model of mammalian neural membrane. Biol. Cybern. 79 (1), 29–37.
Menzler, J., Zeck, G., 2011. Network oscillations in rod-degenerated mouse retinas. J. Neurosci. 31 (6), 2280–2291.
Merigan, W.H., Maunsell, J.H., 1993. How parallel are the primate visual pathways? Annu. Rev. Neurosci. 16, 369–402.
Merrill, D.R., Bikson, M., Jefferys, J.G., 2005. Electrical stimulation of excitable tissue: design of efficacious and safe protocols. J. Neurosci. Methods 141 (2), 171–198.
Muqit, M.M.K., Velikay-Parel, M., Weber, M., Dupeyron, G., Audemard, D., Corcostegui, B., Sahel, J., Le Mer, Y., 2019. Six-month safety and efficacy of the intelligent retinal implant system II device in retinitis pigmentosa. Ophthalmology 126 (4), 637–639.
Nanduri, D., Fine, I., Horsager, A., Boynton, G.M., Humayun, M.S., Greenberg, R.J., Weiland, J.D., 2012. Frequency and amplitude modulation have different effects on the percepts elicited by retinal stimulation. Invest. Ophthalmol. Vis. Sci. 53 (1), 205–214.
Nassi, J.J., Callaway, E.M., 2009. Parallel processing strategies of the primate visual system. Nat. Rev. Neurosci. 10 (5), 360–372.
Naumann, J., 2012. Search for Paradise: A Patient's Account of the Artificial Vision Experiment. Xlibris.
Neumann, E., 1992. Membrane electroporation and direct gene-transfer. Bioelectrochem. Bioenerg. 28 (1–2), 247–267.
Newsome, W.T., Wurtz, R.H., Dursteler, M.R., Mikami, A., 1985. Deficits in visual-motion processing following ibotenic acid lesions of the middle temporal visual area of the macaque monkey. J. Neurosci. 5 (3), 825–840.
Olveczky, B.P., Baccus, S.A., Meister, M., 2003. Segregation of object and background motion in the retina. Nature 423 (6938), 401–408.
Osepchuck, J.M., 1983. Biological Effects of Electromagnetic Radiation. IEEE Press, New York.
Palanker, D.V., 2019. Photovoltaic restoration of sight in age-related macular degeneration. Invest. Ophthalmol. Vis. Sci. 60 (9), 2-2.
Palanker, D., Huie, P., Vankov, A., Aramant, R., Seiler, M., Fishman, H., Marmor, M., Blumenkranz, M., 2004. Migration of retinal cells through a perforated membrane: implications for a high-resolution prosthesis. Invest. Ophthalmol. Vis. Sci. 45 (9), 3266–3270.
Palanker, D., Vankov, A., Huie, P., Baccus, S., 2005. Design of a high resolution optoelectronic retinal prosthesis. J. Neural. Eng. 2, S105–S120.
Pardue, M.T., Stubbs Jr., E.B., Perlman, J.I., Narfstrom, K., Chow, A.Y., Peachey, N.S., 2001. Immunohistochemical studies of the retina following long-term implantation with subretinal microphotodiode arrays. Exp. Eye Res. 73 (3), 333–343.
Passaglia, C.L., Troy, J.B., Ruttiger, L., Lee, B.B., 2002. Orientation sensitivity of ganglion cells in primate retina. Vision Res. 42 (6), 683–694.

Petrusca, D., Grivich, M.I., Sher, A., Field, G.D., Gauthier, J.L., Greschner, M., Shlens, J., Chichilnisky, E.J., Litke, A.M., 2007. Identification and characterization of a Y-like primate retinal ganglion cell type. J. Neurosci. 27 (41), 11019–11027.

Potts, S.E., Schmalz, L., Fenker, M., Diaz, B., Swiatowska, J., Maurice, V., Seyeux, A., Marcus, P., Radnoczi, G., Toth, L., et al., 2011. Ultra-thin aluminium oxide films deposited by plasma-enhanced atomic layer deposition for corrosion protection. J. Electrochem. Soc. 158 (5), C132–C138.

Prevot, P.-H., Lanoë, M., Dalouz, S., Blaize, K., Oubari, O., Gehere, K., Akolkar, H., Buc, G., Picaud, S.A., Sahel, J.A., 2017. Behavioral and electrophysiological characterization of photovoltaic subretinal implants in non-human primates. Invest. Ophth. Vis. Sci. 58 (8), 4270.

Richard, E., Goetz, G., Chichilnisky, E.J., 2015. Recognizing retinal ganglion cells in the dark. Adv. Neurosci. 28.

Rizzo 3rd, J.F., Shire, D.B., Kelly, S.K., Troyk, P., Gingerich, M., McKee, B., Priplata, A., Chen, J., Drohan, W., Doyle, P., et al., 2011. Overview of the boston retinal prosthesis: challenges and opportunities to restore useful vision to the blind. Conf. Proc. IEEE Eng. Med. Biol. Soc. 2011, 7492–7495.

Robblee, L.S., Rose, T.L., 1990. Electrochemical guidelines for selection of protocols and electrode materials for neural stimulation. In: Neural Prostheses: Fundamental Studies, edn. Prentice Hall, Englewood Cliffs, NJ.

Roy, R.K., Lee, K.R., 2007. Biomedical applications of diamond-like carbon coatings: a review. J. Biomed. Mater. Res. B 83b (1), 72–84.

Salzman, C.D., Britten, K.H., Newsome, W.T., 1990. Cortical microstimulation influences perceptual judgements of motion direction. Nature 346 (6280), 174–177.

Schwartz, G.W., Okawa, H., Dunn, F.A., Morgan, J.L., Kerschensteiner, D., Wong, R.O., Rieke, F., 2012. The spatial structure of a nonlinear receptive field. Nat. Neurosci. 15 (11), 1572–1580.

Sekirnjak, C., Hottowy, P., Sher, A., Dabrowski, W., Litke, A.M., Chichilnisky, E.J., 2006. Electrical stimulation of mammalian retinal ganglion cells with multielectrode arrays. J. Neurophysiol. 95 (6), 3311–3327.

Sekirnjak, C., Jepson, L.H., Hottowy, P., Sher, A., Dabrowski, W., Litke, A.M., Chichilnisky, E.J., 2011. Changes in physiological properties of rat ganglion cells during retinal degeneration. J. Neurophysiol. 105 (5), 2560–2571.

Shah, N.P., Madugula, S., Grosberg, L., Mena, G., Tandon, P., Hottowy, P., Sher, A., Litke, A., Mitra, S., Chichilnisky, E.J., 2019. Optimization of electrical stimulation for a high-fidelity artificial retina. In: 2019 9th International IEEE/EMBS Conference on Neural Engineering (NER), pp. 714–718, 20-23 March 2019 2019.

Shannon, C.E., 1998. Communication in the presence of noise (Reprinted from the Proceedings of the IRE, vol 37, pg 10–21, 1949). Proc. IEEE 86 (2), 447–457.

Shen, J., Yang, X., Dong, A., Petters, R.M., Peng, Y.W., Wong, F., Campochiaro, P.A., 2005. Oxidative damage is a potential cause of cone cell death in retinitis pigmentosa. J. Cell. Physiol. 203 (3), 457–464.

Silveira, L.C.L., Heywood, C.A., Cowey, A., 1987. Contrast sensitivity and visual-acuity of the pigmented rat determined electrophysiologically. Vision Res. 27 (10), 1719–1731.

Sim, S.L., Szalewski, R.J., Johnson, L.J., Akah, L.E., Shoemaker, L.E., Thoreson, W.B., Margalit, E., 2014. Simultaneous recording of mouse retinal ganglion cells during epiretinal or subretinal stimulation. Vision Res. 101, 41–50.

Smith, W., Assink, J., Klein, R., Mitchell, P., Klaver, C.C., Klein, B.E., Hofman, A., Jensen, S., Wang, J.J., de Jong, P.T., 2001. Risk factors for age-related macular degeneration: pooled findings from three continents. Ophthalmol. 108 (4), 697–704.

Sramek, C., Paulus, Y., Nomoto, H., Huie, P., Brown, J., Palanker, D., 2009. Dynamics of retinal photocoagulation and rupture. J. Biomed. Opt. 14 (3), 034007.

Stingl, K., Bartz-Schmidt, K.U., Gekeler, F., Kusnyerik, A., Sachs, H., Zrenner, E., 2013. Functional outcome in subretinal electronic implants depends on foveal eccentricity. Invest. Ophthalmol. Vis. Sci. 54 (12), 7658–7665.

Stingl, K., Bartz-Schmidt, K.U., Besch, D., Chee, C.K., Cottriall, C.L., Gekeler, F., Groppe, M., Jackson, T.L., MacLaren, R.E., Koitschev, A., et al., 2015. Subretinal visual implant Alpha IMS–clinical trial interim report. Vision Res. 111 (Pt B), 149–160.

Stingl, K., Schippert, R., Bartz-Schmidt, K.U., Besch, D., Cottriall, C.L., Edwards, T.L., Gekeler, F., Greppmaier, U., Kiel, K., Koitschev, A., et al., 2017. Interim results of a multicenter trial with the new electronic subretinal implant Alpha AMS in 15 patients blind from inherited retinal degenerations. Front. Neurosci. 11, 445.

Strauss, O., Stumpff, F., Mergler, S., Wienrich, M., Wiederholt, M., 1998. The Royal College of Surgeons rat: an animal model for inherited retinal degeneration with a still unknown genetic defect. Acta Anat. 162 (2–3), 101–111.

Thibos, L.N., Levick, W.R., 1983. Bimodal receptive fields of cat retinal ganglion cells. Vision Res. 23 (12), 1561–1572.

Tochitsky, I., Polosukhina, A., Degtyar, V.E., Gallerani, N., Smith, C.M., Friedman, A., Van Gelder, R.N., Trauner, D., Kaufer, D., Kramer, R.H., 2014. Restoring visual function to blind mice with a photoswitch that exploits electrophysiological remodeling of retinal ganglion cells. Neuron 81 (4), 800–813.

Tsai, D., Morley, J.W., Suaning, G.J., Lovell, N.H., 2009. Direct activation and temporal response properties of rabbit retinal ganglion cells following subretinal stimulation. J. Neurophysiol. 102 (5), 2982–2993.

Vaney, D.I., Sivyer, B., Taylor, W.R., 2012. Direction selectivity in the retina: symmetry and asymmetry in structure and function. Nat. Rev. Neurosci. 13 (3), 194–208.

Victor, J.D., Shapley, R.M., 1979. The nonlinear pathway of Y ganglion cells in the cat retina. J. Gen. Physiol. 74 (6), 671–689.

Wandell, B., 1995. Foundations of Vision. Sinauer Associates, Inc., Sunderland, MA.

Wang, G.X., Liu, W.T., Sivaprakasam, M., Kendir, G.A., 2005. Design and analysis of an adaptive transcutaneous power telemetry for biomedical implants. IEEE Trans. Circuits Syst. I. 52 (10), 2109–2117.

Wassle, H., 2004. Parallel processing in the mammalian retina. Nat. Rev. Neurosci. 5 (10), 747–757.

Weiland, J.D., Anderson, D.J., 2000. Chronic neural stimulation with thin-film, iridium oxide electrodes. IEEE Trans. Biomed. Eng. 47 (7), 911–918.

Weiland, J.D., Shyu, J.S., Margalit, E., Chen, S.J., D'Anna, S.A., Suzuki, S., Humayun, M.S., de Juan, E., 2000. Electrical stimulation of the retina in normal and retinal degenerate dog. Invest. Ophthalmol. Vis. Sci. 41 (4), S888.

Weiland, J.D., Anderson, D.J., Humayun, M.S., 2002. In vitro electrical properties for iridium oxide versus titanium nitride stimulating electrodes. IEEE Trans. Biomed. Eng. 49 (12), 1574–1579.

Weitz, A.C., Nanduri, D., Behrend, M.R., Gonzalez-Calle, A., Greenberg, R.J., Humayun, M.S., Chow, R.H., Weiland, J.D., 2015. Improving the spatial resolution of epiretinal implants by increasing stimulus pulse duration. Sci. Transl. Med. 7 (318), 318ra203.

Werginz, P., Rattay, F., 2016. The impact of calcium current reversal on neurotransmitter release in the electrically stimulated retina. J. Neural. Eng. 13 (4), 046013.

Werginz, P., Benav, H., Zrenner, E., Rattay, F., 2015. Modeling the response of ON and OFF retinal bipolar cells during electric stimulation. Vision Res. 111 (Pt B), 170–181.

Wong, W.L., Su, X., Li, X., Cheung, C.M., Klein, R., Cheng, C.Y., Wong, T.Y., 2014. Global prevalence of age-related macular degeneration and disease burden projection for 2020 and 2040: a systematic review and meta-analysis. Lancet Glob. Health 2 (2), e106–e116.

Zoccolan, D., 2015. Invariant visual object recognition and shape processing in rats. Behav. Brain Res. 285, 10–33.

Zrenner, E., Bartz-Schmidt, K.U., Benav, H., Besch, D., Bruckmann, A., Gabel, V.P., Gekeler, F., Greppmaier, U., Harscher, A., Kibbel, S., et al., 2011. Subretinal electronic chips allow blind patients to read letters and combine them to words. Proc. Biol. Sci. 278 (1711), 1489–1497.